

## RESEARCH ARTICLE

# Process-oriented evaluation of the oversea AROME configuration: Focus on the representation of cloud organisation

Florent Beucher<sup>1</sup>  | Fleur Couvreur<sup>1</sup>  | Dominique Bouniol<sup>1</sup>  |  
Ghislain Faure<sup>1</sup> | Florence Favot<sup>1</sup> | Thibaut Dauhut<sup>1</sup>  | Alex Ayet<sup>2,3</sup> 

<sup>1</sup>Météo-France, CNRM-GAME/GMME, Toulouse, France

<sup>2</sup>CNRS, Université Grenoble Alpes, Inria, Grenoble INP, GIPSA-Lab, LOPS, Grenoble, France

<sup>3</sup>CECI, Université de Toulouse, CNRS, CERFACS, Toulouse, France

## Correspondence

F. Beucher, Météo-France, CNRM-GAME/GMME, Toulouse, France.  
Email: [florent.beucher@meteo.fr](mailto:florent.beucher@meteo.fr)

## Abstract

This study evaluates the ability of the French convection-permitting model AROME-OM to represent shallow cumulus and their main organisations for boreal winter conditions in the North Atlantic trades. It uses a set of three winter seasons (January–February, 2018–2020) of high-resolution (1.3 and 2.5 km) simulations over the Caribbean domain (9.7–22.9°N, 75.3–51.7°W). The model is assessed against soundings at Grantley Adams Airport and remote-sensing observations at a site located on the east coast of Barbados which is representative of downwind trade regimes. The thermodynamic environment of the model fits the observations overall but the boundary layer is slightly too deep, resulting in a weak cold and dry bias. Both model and observations clearly exhibit (a) a double peak of cloud fraction, a first peak near the cloud base and a second one near the cloud top and (b) a larger variance in cloudiness near the top of the deepest cumuli, at around 2 km, with a higher sensitivity to the environment. We then take advantage of the EUREC<sup>4</sup>A field campaign which took place in January–February 2020 to assess the ability of the model to reproduce the four main mesoscale patterns and to characterize the air masses in which they develop. All the observations confirm the capacity of the model to predict the different mesoscale organizations and their associated environment.

## KEYWORDS

cloud resolving model, clouds-organisation, evaluation, North Atlantic Trades, shallow convection

## 1 | INTRODUCTION

Subtropical oceanic fair-weather cumuli are ubiquitous across the downwind trade regions. There is a growing need to better understand the key mechanisms that regulate those clouds, which play a critical role in the boundary-layer dynamics and the global climate. Over the past two decades, parametrizations of shallow convection in general circulation models have improved

greatly (Tiedtke, 1989; Hourdin *et al.*, 2002; Rio and Hourdin, 2008; Pergaud *et al.*, 2009) but it is still a challenge to better represent the distribution of fair-weather cumuli and their organisation, especially over the subtropical oceans. The strong impact of trade-wind cumuli on the radiation balance, even if they are small and short-lived, represents a source of uncertainty in climate projections with a wide variety of responses among climate models (Sherwood *et al.*, 2014; Nuijens *et al.*, 2015).

Trade-wind regions are widespread and their thermodynamic large-scale environments show significant variability across tropical oceans. Fields of broken cumulus rather populate western sides of the oceans whilst over eastern sides the appearance of the clouds resemble open and closed cells. These variations of low-level cloudiness cannot be explained by a single strong predictor but are rather controlled by the combined effect of various parameters. A regime of downstream trades is dominated by relatively weak trade-wind inversion, variable subsidence at 500 hPa, deep trade-wind layer and warm sea-surface temperature (SST) ranging between 26 and 28 °C (Figure 1a) (Bony *et al.*, 2004; Medeiros and Nuijens, 2016). Based on satellite observations, Stevens *et al.* (2020) have identified in this region four prominent mesoscale patterns known as Sugar, Gravel, Flower and Fish, which distinguish themselves by their spatial organisation and the variation of their cloud-top cloudiness. A significant dependence of these mesoscale cloud patterns on surface wind speed and trade-wind inversion strength (measured by the lower-tropospheric stability, LTS, defined as  $\theta_{700} - \theta_{1000}$ , where  $\theta$  is the potential temperature: Klein and Hartmann, 1993) has been found by Bony *et al.* (2020). These relationships have been confirmed by Schulz *et al.* (2021) with the help of a neural network in order to classify the four patterns (Rasp *et al.*, 2020). Janssens *et al.* (2021) have shown that these organisations are associated with the distribution extremes of organisations' metrics which explains why they are easily distinguishable to the human eye but they do not allow the spanning of the large variety of other organisations.

Simulations of the shallow convection remain a challenge since models must be able to represent the subtle relationship between clouds and environment with typical cloud size representing only a fraction of a model grid box. Recently, Heim *et al.* (2021) shed light on the benefits of using kilometre-scale models – so-called convection-permitting models (CPM) – to simulate shallow convection with an ability to partially resolve the interactions between clouds and their environment. However, a large variability in the cloud simulation among the different models could still be noted. The main goal of this work is to evaluate the ability of the overseas configuration of the French CPM Applications of Research to Operations at Mesoscale (AROME: Seity *et al.*, 2011), the so-called AROME-OM (Faure *et al.*, 2020), to represent the shallow convection at a kilometre resolution. Past studies have shown the good capacity of AROME to reproduce the life cycle of mesoscale convective systems during the West African monsoon (Beucher *et al.*, 2014; Ricard *et al.*, 2020) but few focused on a maritime tropical domain, in particular for the operational version (Faure *et al.*, 2020).

The scarcity of the observations in the Caribbean domain (Figure 1a) represents a major hindrance for the evaluation of AROME-OM. The EUREC<sup>4</sup>A (Elucidating the role of clouds-circulation coupling in climate) campaign which took place to the east of Barbados in January–February 2020 (Stevens *et al.*, 2021) represents an opportunity in that regard since it provides a battery of supplementary observations (in addition to routine soundings). Remote-sensing instruments installed since 2010 at the Barbados Cloud Observatory (BCO, Figure 1b)

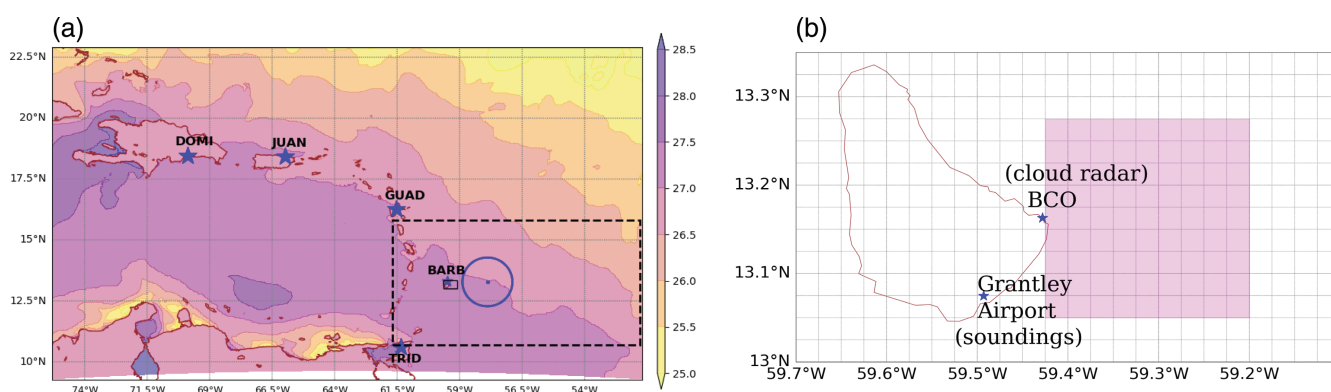


**FIGURE 1** (a) Map of the Caribbean domain ( $1,200 \times 2,000 \text{ km}^2$ ) of AROME-OM with blue stars indicating available radiosoundings (DOMI for Santo Domingo, JUAN for San Juan, GUAD for Guadeloupe, BARB for Grantley Adams Airport, TRID for Trinidad and Tobago). The black dashed box indicates the focus domain ( $500 \times 1,000 \text{ km}^2$ ) for the evaluation of AROME-OM. The blue circle represents the HALO circle path along which dropsondes are released during the EUREC<sup>4</sup>A campaign. The thin black rectangle is the zoom shown in (b). In the background the mean AROME-OM SST averaged over the EUREC<sup>4</sup>A period (January–February 2020) is displayed. (b) Zoom over Barbados Island with radiosoundings launched at Grantley Adams Airport, and the Barbados Cloud Observatory (BCO) equipped with various remote-sensor instruments such as the cloud radar. The 81 pink mesh grids represent the size of the effective resolution of AROME-OM which is about 9 times its native grid (2.5 km) (see details in Section 2.3) [Colour figure can be viewed at [wileyonlinelibrary.com](https://onlinelibrary.wiley.com)]

(Stevens *et al.*, 2016) provide insight into the vertical distribution of cloud fraction. Analysing these data, Nuijens *et al.* (2014) found a double peak structure with a first peak at 1 km near the cloud base and a second one slightly below 2 km with the development of a stratiform cloud layer under the trade-wind inversion. Unlike coarser global models (Nuijens *et al.*, 2015), the double peak of cloud fraction is rather well captured by the large-eddy simulation (LES: Stevens *et al.*, 2001; Narenpitak *et al.*, 2021), particularly when environment is characterized by a strong trade-wind inversion (Vogel *et al.*, 2020).

Motivated by these past studies, this article addresses the following questions: to what extent, under a regime of a weak trade-wind inversion, is AROME-OM able to simulate this double peak while the shallow convection is still parametrized? And in which environment is the vertical distribution of the cloud fraction the most sensitive? We also investigate how AROME-OM is able to capture the four main spatial mesoscale organisations (Stevens *et al.*, 2020) and their associated large-scale environment focusing on four typical case-studies selected during the EUREC<sup>4</sup>A period.

In the following, we give a short description of the data used, along with the configuration of AROME-OM (Section 2). In Section 3, we assess the ability of the model to capture the double peak of cloud fraction and its dependence on the large-scale environment. This is followed in Section 4 by the evaluation of the model to reproduce the main mesoscale patterns of Stevens *et al.* (2020) which is based on four case-studies. Finally, the main results are outlined and perspectives provided by such a CPM for further investigations of the interplay of mechanisms leading to mesoscale organisation changes are discussed.

## 2 | MODEL CONFIGURATION AND OBSERVATIONS FOR ITS EVALUATION

### 2.1 | Configuration of AROME-OM

Since 2016, AROME-OM has been run across the French overseas territories at a 2.5 km horizontal grid spacing four times a day with a 48 hr forecast range (Faure *et al.*, 2020). This study focuses on forecasts starting at 0000 UTC. We discard the first 6 hr in order to avoid the initial spin-up phase and only use the 6 to 30 hr forecast ranges. The AROME-OM system is basically a downscale, without any additional data assimilation, of the deterministic global model Integrated Forecast System (IFS) of the European Centre for Medium-Range Weather Forecasts (ECMWF). The model is forced on its lateral boundaries at an hourly frequency (Faure *et al.*, 2020). It uses 90 vertical levels

with 41 levels below 700 hPa. The continental surface initial fields are taken from the global model ARPEGE (Action des Recherche Petite Echelle et Grande Echelle), which uses the same surface model as AROME-France, known as SURFEX (Masson *et al.*, 2013). The SST are initialized by the Mercator global model PSY4 at 1/12° (Lellouche *et al.*, 2018) and since 2017 AROME-OM has been coupled with a one-dimensional (1D) vertical Mixed-Layer Ocean Model (CMO) (Lebeaupin Brossier *et al.*, 2009). AROME-OM has no specific tuning of its physical parametrizations compared to the AROME configuration (see details in Seity *et al.* (2011)). Note that at a 2.5 km grid spacing, the deep convection is permitted but the shallow convection is parametrized by a mass-flux scheme based on a stationary bulk updraught (Pergaud *et al.*, 2009).

The assessment of AROME-OM is carried out over the French Caribbean domain (9.7°N–22.9°N, 75.3°W–51.7°W, 1,200 × 2,000 km<sup>2</sup>) (Figure 1a). The evaluation focuses on the southeastern part of this domain (Figure 1a, black dashed box, 500 × 1,000 km<sup>2</sup>) where the EUREC<sup>4</sup>A campaign mainly took place. An additional forecasting set-up of AROME-OM at a 1.3 km horizontal grid spacing, the near-future operational configuration, was also performed specifically during EUREC<sup>4</sup>A. This simulation was re-gridded at a 2.5 km resolution to ensure a fair comparison with the operational configuration. Evaluation of this future configuration is focused on in Section 4.3.

### 2.2 | Evaluation procedure

The evaluation of AROME-OM at a 2.5 km resolution spans three winter seasons (January–February) from 2018 to 2020 which ensures that a wide variety of large-scale environments are sampled. This evaluation is carried out against data collected at both Grantley Adams Airport (13.07°N, 59.49°W) and the BCO platform (Stevens *et al.*, 2016) (Figure 1b) which is representative of a downwind trade regime where broken shallow cumuli prevail (Medeiros and Nuijens, 2016). The dropsondes (George *et al.*, 2021) that have been released along a circle by the High Altitude and Long range research (HALO) aircraft during the EUREC<sup>4</sup>A campaign are also used for this evaluation. Datasets used for the evaluation procedure are summarized in Table 1.

### 2.3 | The BCO platform

In addition to standard surface meteorological measurements at 2 m above ground (wind, temperature, humidity),

TABLE 1 Set of data used for the evaluation of AROME-OM

| Parameter                     | Instrument                    | Period                             | Resolution OBS<br>AROME-OM  | Number<br>(* with low-pass filter) |
|-------------------------------|-------------------------------|------------------------------------|---|------------------------------------|
| Cloud fraction<br>(z profile) | Cloud radar and<br>ceilometer | Jan/Feb, 2018–2020                 | BCO<br>2.5 km   |                                    |
| Cloud fraction (x, y)         | GOES16 + SAFNWC               | 4 case-studies                     | 2 km × 2 km<br>2.5 and 1.3 km                                     | Figures 9 and S1                   |
| Accumulated rainfall          | Rain-gauge                    | Jan/Feb, 2018–2020                 | BCO<br>Square ahead of BCO<br>(22.5 × 22.5 km <sup>2</sup> )      | Figure 7                           |
| PW (x, y)                     | AMSR2                         | 4 case-studies                     | 25 km × 25 km<br>2.5 and 1.3 km                                   | Figure 10                          |
| PW                            | GNSS radiometer<br>HATPRO     | Jan/Feb 2020<br>Jan/Feb, 2018–2020 | BCO BCO<br>2.5 km   | Figures 6* and 7                   |
| u2m                           | Anemometer                    | Jan/Feb, 2018–2020                 | BCO<br>2.5 km   | Figures 6* and 7                   |
| t2m                           | Thermometer                   | Jan/Feb, 2018–2020                 | BCO<br>2.5 km   | Figures 6* and 7                   |
| Wind speed, T, qv             | Sounding                      | Jan/Feb, 2018–2020                 | Airport<br>2.5 km   |                                    |
| T, U, qv, VV                  | Dropsonde                     | 4 case-studies                     | Mean over Halo circle<br>(12 dropsondes)<br>Mean over Halo circle |                                    |

the Max Planck Institute for Meteorology has installed at the BCO supersite (<https://barbados.mpimet.mpg.de>) various advanced vertically pointing remote-sensing devices. Vertical profiles of hydrometeors (cloud and rain) are derived using the COmbined Radar And Lidar instrument (CORAL) Ka-band cloud radar with a profile every 10 s and a vertical resolution of 30 m up to 18 km. The high sensitivity of  $-55$  dBZ at 5 km height for a 10 s averaging time, below which radar reflectivity is filtered, allows us to detect a wide spectrum of clouds in the entire troposphere (Görsdorf *et al.*, 2015). For a fair comparison with AROME-OM, the cloud radar profile (605 regular levels) is re-gridded on the model vertical grid (90 levels). A roughly 30 min temporal averaging of the cloud radar profiles is applied in order to match the horizontal scale resolved by the model (Hogan *et al.*, 2001; Bouniol *et al.*, 2010). This averaging time is computed by estimating the required time for an air parcel to cross the length of the effective horizontal resolution of the model advected by the horizontal wind. The effective resolution is impacted by the implicit diffusion of the semi-implicit semi-Lagrangian scheme used in AROME (Malardel and Ricard, 2015) and has been estimated as about nine times its native grid spacing (Ricard *et al.*, 2013). To suppress echoes of rain below cloud base,

cloud base height and rain flag (rain-rate  $>0.05$  mm·hr<sup>-1</sup>) are derived using ceilometer and micro-rain radar (see details in Nuijens *et al.* (2014)). The occurrence of cloud is only considered when cloud fraction is above 0.01.

Two different instruments are used for precipitable water (PW): a ground-based microwave radiometer was installed in 2018 (Schnitt *et al.*, 2020), followed by a ground-based Global Navigation Satellite System (GNSS) BCON (BCO North) station in 2020 (Bock *et al.*, 2021). These datasets are valuable for an evaluation of AROME-OM since they are not assimilated by its forcing IFS model, with the caveat that the BCON GNSS shows a dry bias of 1.6 mm compared to the BCO sondes (Bock *et al.*, 2021).

## 2.4 | Grantley Adams Airport soundings

Within the Caribbean domain, five twice-daily (1100 UTC and 2300 UTC) radiosoundings launched from Santo Domingo, San Juan, Le Raizet (Guadeloupe), Grantley Adams Airport (Barbados), and Trinidad and Tobago (Figure 1a, blue stars) are assimilated into the IFS 4D system. Within the domain targeted in this study, only

the sounding of Barbados Airport ( $\sim 5,000$  vertical levels) remains for the assessment of the vertical thermodynamical profiles of AROME-OM. The airport is located at an altitude of 52 m in the southern part of the island, a few hundred metres away from the sea. It is located on the lee side of the trade winds which may differ slightly from “pure” maritime conditions. The nearest grid point of the airport in AROME-OM is located 900 m southwards at an altitude of 32 m allowing an evaluation with a good accuracy. During EUREC<sup>4</sup>A, soundings were also launched at the BCO but the period is not long enough for the evaluation of AROME-OM thermodynamics.

## 2.5 | EUREC<sup>4</sup>A dropsondes

During EUREC<sup>4</sup>A, additional vertical profiles are provided by the release of about 12 dropsondes (George *et al.*, 2021) along each HALO circle. The HALO circle path (Figure 1a, blue circle) extends between 12.3°N and 14.3°N (Konow *et al.*, 2021), centred approximately 1° westwards of the BCO. To mimic the observations, the AROME-OM outputs have been averaged along the circle. The evaluation of the parameters near the surface is carried out at 1,000 hPa since data from dropsondes are sometimes not available below this level. The dropsondes have also been used to compute the vertical velocity from the divergence of the horizontal wind over the entire circle (Bony and Stevens, 2019). For its evaluation, the simulated vertical velocity has also been averaged over the entire circle in AROME-OM to ensure a fair comparison.

## 2.6 | Satellite observations

In order to document the spatial variability, the dataset is complemented by observations provided by spaceborne sensors, in particular from the visible channel 2 of the Advanced Baseline Imager on board the geostationary satellite GOES16. The satellite measures reflectance at a  $0.5 \text{ km} \times 0.5 \text{ km}$  resolution and a 10-minute temporal frequency. The combination of this reflectance and of a  $2 \text{ km} \times 2 \text{ km}$  cloud mask from the Nowcasting Satellite Application Facilities (SAFNWC) allows us to construct a gridded field of cloud fraction at a  $2 \text{ km} \times 2 \text{ km}$  resolution. This gridded field accounts for partial cloudiness inside a grid point instead of using a binary cloudiness flag. The evaluation of the low- and mid-cloud cover (up to 450 hPa) of AROME-OM and IFS is carried out against this reconstructed field.

To estimate PW, Advanced Microwave Scanning Radiometer 2 (AMS2) measurements (Imaoka *et al.*, 2010) on board the Global Change Observation

Mission–Water (GCOM–W1) satellite at a spatial resolution of about  $25 \text{ km} \times 25 \text{ km}$  are also used. PW is retrieved from four AMS2 channels through a statistical algorithm. Errors on the PW retrieved from the AMS2 family are expected to be lower than 1 mm (Wentz and Meissner, 2000).

## 3 | ABILITY OF AROME-OM TO REPRESENT THE WINTERTIME SHALLOW CONVECTION

### 3.1 | Evaluation of the thermodynamical profiles

Figure 2 compares the wintertime composite soundings of 2300 UTC over the three considered winters (January–February, 2018–2020) with the vertical profiles of AROME-OM and of the IFS model. The vertical profiles at 1100 UTC are not shown since they exhibit roughly the same biases. Both potential temperature and specific humidity profiles show too deep a sub-cloud layer (SCL) in AROME-OM with a top located too high ( $\sim 920 \text{ hPa}$ ) compared to the observations ( $\sim 940/950 \text{ hPa}$ ). This shortcoming also partly explains why AROME-OM is too dry ( $-1 \text{ g}\cdot\text{kg}^{-1}$ ) in the sub-cloud layer and too cold in the cloud layer ( $-0.5 \text{ K}$  between 930 and 800 hPa). In contrast to AROME-OM, the SCL is too thin in IFS compared to the observations, suggesting that the forcing model does not control the thickness of the SCL in AROME-OM. It is hypothesized rather that the shallow convection scheme (Pergaud *et al.*, 2009) of AROME has to be tuned in order to reduce the strength of the updraught or to adjust the entrainment/detrainment rates at the top of the SCL. The overestimation of the wind speed ( $+1$  to  $+2 \text{ m}\cdot\text{s}^{-1}$ ) in AROME-OM up to the trade-wind inversion ( $\sim 800 \text{ hPa}$ ) could be partly driven by IFS as it roughly shows identical biases. This overestimation of the trade winds in IFS has been recently confirmed by Savazzi *et al.* (2022) by using sondes that have not been assimilated by IFS. Note that the 95% confidence interval of each environmental profile (OBS and AROME) is rather weak which underlines the low intraseasonal variability of the large-scale environment in which subtropical shallow convection forms. Evaluation at the other sounding sites in the Caribbean domain indicate similar biases. A simulation of AROME-OM recently run over a vast domain from Barbados to Cape Verde during the period of EUREC<sup>4</sup>A shows similar biases suggesting that the thermodynamics biases are rather linked to AROME physical parametrizations than associated with the biases of the forcing model. In the following sections, besides these existent biases, albeit weak, we analyse the ability of AROME-OM to represent

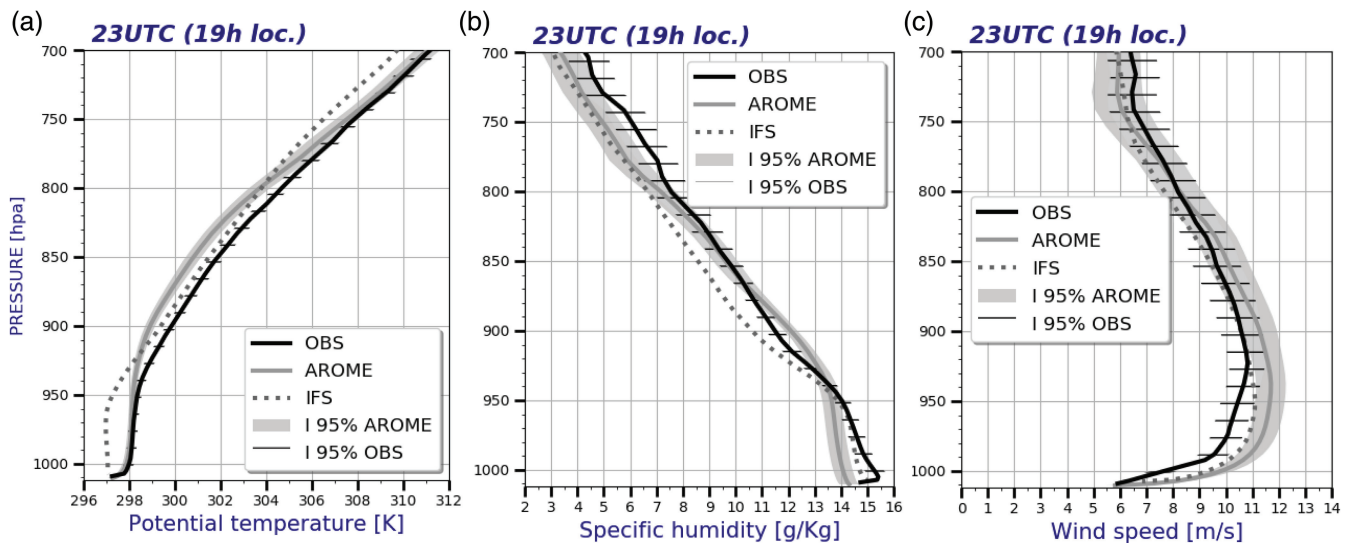


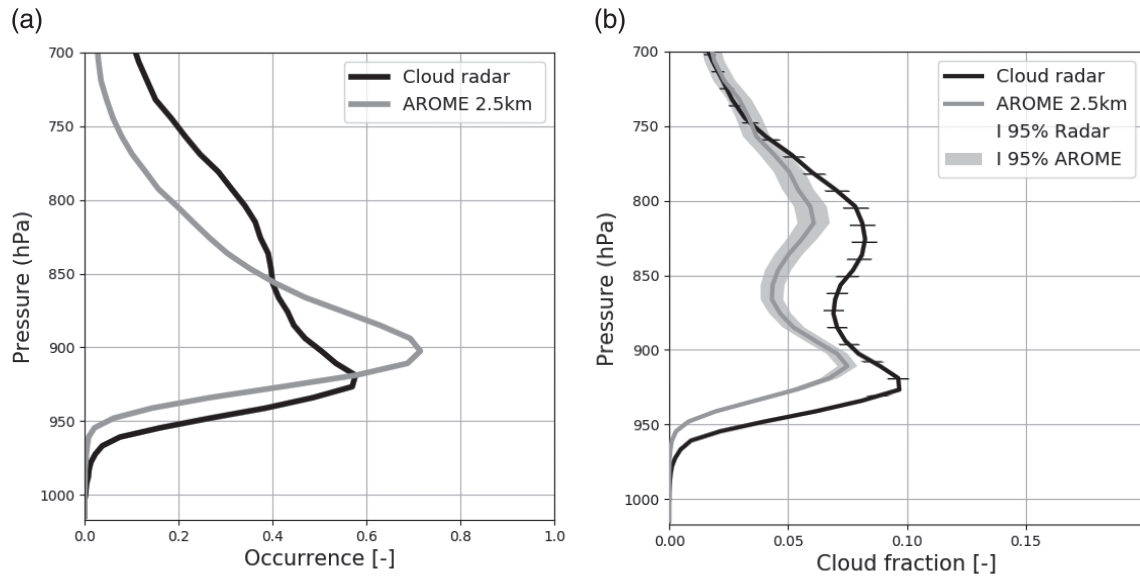
**FIGURE 2** Mean vertical profiles (January–February, 2018–2020) at 2300 UTC at Grantley Adams Airport of the (a) potential temperature (K), (b) specific humidity ( $\text{g}\cdot\text{kg}^{-1}$ ), and (c) wind speed ( $\text{m}\cdot\text{s}^{-1}$ ) for the radiosoundings (full dark line), AROME-OM (grey full line) and IFS (grey dashed line) models. The 95% interval confidence is displayed with black horizontal lines for the radiosoundings and with grey shading for AROME-OM [Colour figure can be viewed at [wileyonlinelibrary.com](http://wileyonlinelibrary.com)]

the shallow convection in terms of vertical and horizontal distributions.

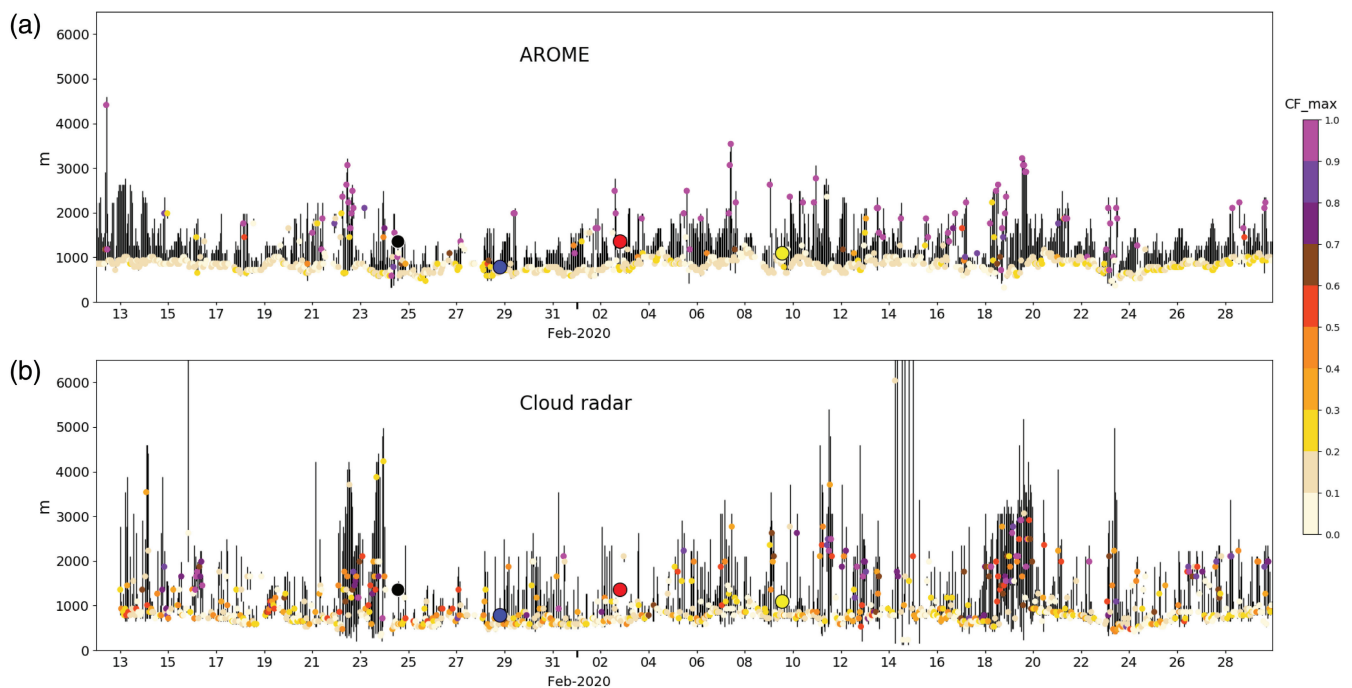
### 3.2 | Evaluation of the cloud fraction

Figure 3 shows an evaluation that spans the three considered winters (January–February, 2018–2020) of the vertical distribution of the cloud fraction and of its occurrence frequency at the BCO point. For a fair comparison with the AROME-OM hourly snapshots, cloud radar profiles are averaged in time and vertically re-gridded (details in Section 2.3). The AROME-OM vertical profile of cloud occurrence (Figure 3a) fits well with the observed one, with a peak frequency of about 60–70% near the cloud base, 900 hPa for AROME-OM and 920 hPa for the radar. As discussed in the previous section, too thick and too cold an SCL explains why the cloud base is located too high in the model. The radar profile shows a secondary peak of occurrence frequency at about 820 hPa which is not simulated by the model (Figure 3a). In contrast, when focusing on situations of cloud occurrence (Figure 3b), the cloud fraction of the secondary peak is well represented by AROME-OM with values reaching 0.06. It demonstrates the ability of AROME-OM to mimic stratiform-like clouds, although the occurrence of such clouds is significantly underestimated (Figure 3a). The temporal evolution of the cloud depth during EUREC<sup>4</sup>A shows that AROME-OM (Figure 4a) constructs two distinct modes of shallow convection: (a) a first one, the most frequent, made of very shallow convection (VSC) with

a peak cloud fraction of about 0.15 near the cloud base, and (b) a second one made of more vertically developed shallow convection (VDSC) with saturated cloud fraction (magenta dot) near the cloud top. This latter feature illustrates that the updraught associated with the cloud can cover the whole grid point. Indeed, at a 2.5 km resolution the shallow convection, in particular the stratiform one, is partially resolved (Honnert, 2016). As displayed in Figure 4b, the VSC mode is well observed in the cloud radar with a peak of occurrence of the maximum of cloud fraction located near the cloud base, although values are slightly stronger (0.2–0.3) than in AROME-OM. The VDSC mode exhibits divergent characteristics from AROME-OM with clouds more vertically developed, the maximum of cloud fraction being instead located a few hundred metres below the cloud top with a much more variable magnitude, from 0.3 to 1. For instance, from 22 to 24 January 2020, the cloud top can exceed 4,500 m in the observations and drops to 3,000 m in AROME-OM. The distribution of the height of the base and the top of the cloud over the three winter seasons (Figure 5) confirms that AROME-OM shows a better ability to simulate the base than the depth of the cloud. When small cloud fraction ( $<0.1$ ) is filtered (Figure 5b, right), the second peak in the distribution of the cloud-top heights is well captured by AROME-OM. Overall, we may argue that in spite of biases in the SCL, AROME-OM is able to simulate the double peak structure of the shallow cumulus, with the caveat that the occurrence of the second peak is underestimated and associated with an excessive cloud fraction when present.



**FIGURE 3** Mean vertical profiles (January–February, 2018–2020) at the BCO of (a) the cloud occurrence frequency, and (b) the cloud fraction when there is occurrence. The CORAL cloud radar is displayed in black and AROME-OM in grey



**FIGURE 4** (a,b) Temporal evolution at the BCO of the cloud during EUREC<sup>4</sup>A at an hourly frequency. The vertical lines represent the vertical extension of the cloud. The dots represent the location of the maximum of the cloud fraction with colour indicating its value ranging between 0 and 1. Coloured dots (black, blue, red, yellow) represent the four case-studies (fish, sugar, flower, gravel) detailed in Section 4 [Colour figure can be viewed at [wileyonlinelibrary.com](http://wileyonlinelibrary.com)]

### 3.3 | Dependence of the cloud fraction on the large-scale environment

To gain further insight into how the large-scale environment affects trade-wind cloudiness, this section investigates the cloud fraction sensitivity to key controlling

parameters such as 2 m temperature ( $t_{2m}$ ), 2 m zonal wind speed ( $u_{2m}$ ), and PW. Figure 6 shows the mean profile of cloud fraction associated with the 20% lowest (resp. highest) parameter values as well as for 60% of intermediate parameter values. These calculations are carried out only for common dates between observations and AROME-OM

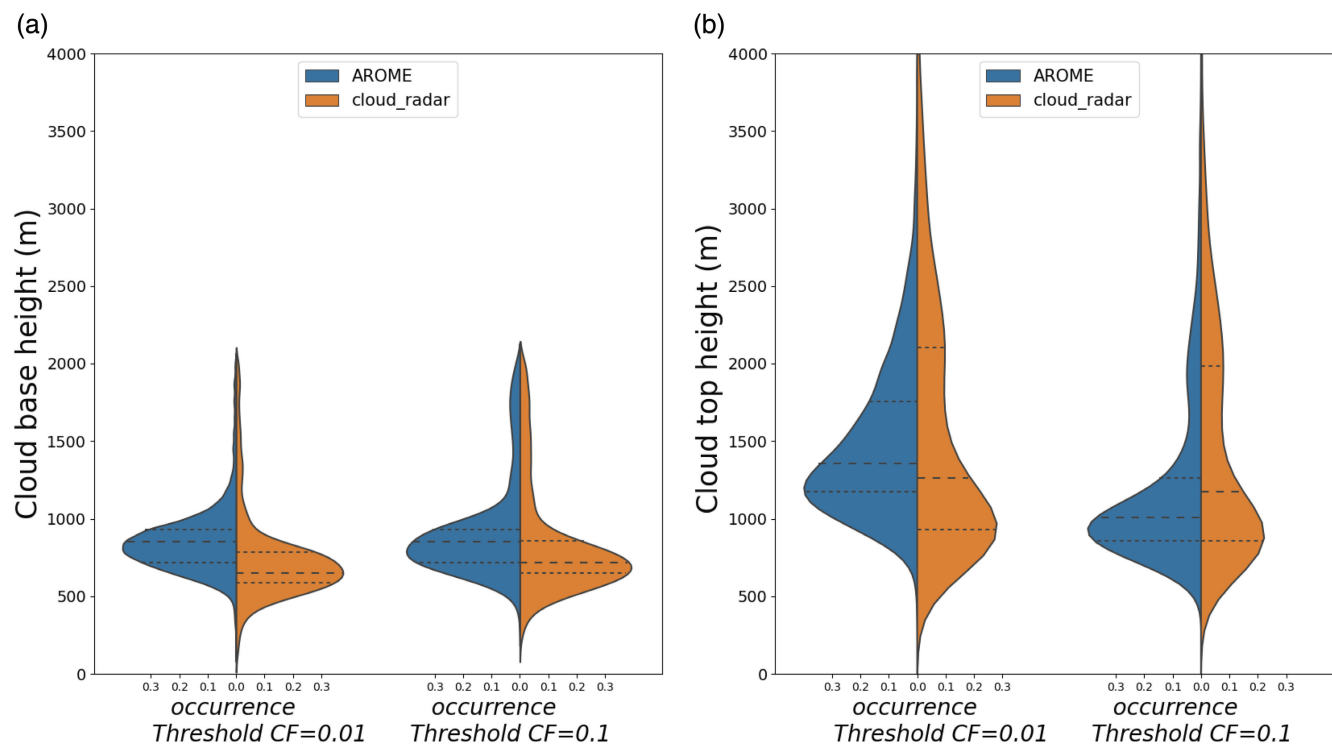


**FIGURE 5** Occurrence distribution over three winter periods (January–February, 2018–2020) at the BCO for AROME-OM (in blue) and the cloud radar (in brown) of (a) the cloud base height and (b) the cloud top height, for two different thresholds (0.01 and 0.1) below which cloud fraction is masked. The two dotted lines represent the first and last quartile and the dashed line the median of each distribution [Colour figure can be viewed at [wileyonlinelibrary.com](http://wileyonlinelibrary.com)]

in order to characterize similar environments. The spread between the 20% lowest and 20% highest of each parameter is rather weak (see values in the figure legends), highlighting the low variability of the environment over this maritime subtropical domain; 60% of values are within 1 K for the  $t_{2m}$ ,  $3 \text{ m}\cdot\text{s}^{-1}$  for  $u_{2m}$ , and 9 mm for the PW.

The large cloud fractions near 800 hPa (Figure 6, upper panel) are associated with cold  $t_{2m}$  and high PW in observations and AROME-OM but are not really sensitive to the surface wind speed. To better investigate the role played by the large-scale environment, the high-frequency variability of  $t_{2m}$ ,  $u_{2m}$  and PW has been removed by a low-pass filter of 48 hr (Figure 6, lower panel). The cloud base in the observations is particularly sensitive to synoptic fluctuations in  $u_{2m}$  and PW (Figure 6e,f). An increase of  $u_{2m}$  leads to a moistening in the sub-cloud layer and an increase of cloudiness near the level of free condensation. The failure of the model in reproducing this sensitivity could not be linked with the biases identified in the SCL since near the surface, wind speed roughly fits the observations (Figure 7). More in-depth studies are necessary to disentangle the implied physical mechanisms, but mesoscale circulations associated with more vertically developed cumulus or strength of the surface moisture flux could be misrepresented at a 2.5 km grid spacing. It

is worth mentioning that at the strongest  $u_{2m}$  the model shows rather a good ability to reproduce the deepening of the cloud above 800 hPa (dotted lines, Figure 6b,e), which confirms the findings of Nuijens and Stevens (2012).

The second peak of cloudiness is the most influenced by large-scale environments, with enhanced cloudiness on the days that are the coolest (Figure 6d). This second peak is also influenced by fluctuations of large-scale PW (Figure 6f), suggesting that a drier environment favours stronger trade-wind inversion. In contrast, on the days that are the hottest, the cloudiness near 800 hPa decreases. This is consistent with the findings of Schulz *et al.* (2021), showing that stratiform-like structure rather originates from midlatitudes (low  $t_{2m}$ ) whilst variable vertically extensive structure is consistent with a more tropical influence (high  $t_{2m}$ ) (their figures 6 and 10). Note that when PW is not filtered (Figure 6c), PW and cloud depth are strongly correlated since PW corresponds to the local footprint of the clouds.

Overall, it may be argued that the sensitivity of the large-scale environment is captured more by the model at the cloud-top height than at the cloud base, suggesting that the subtle relationship between clouds and environment is better represented at the level of the trade-wind inversion than in the sub-cloud layer or near the surface.

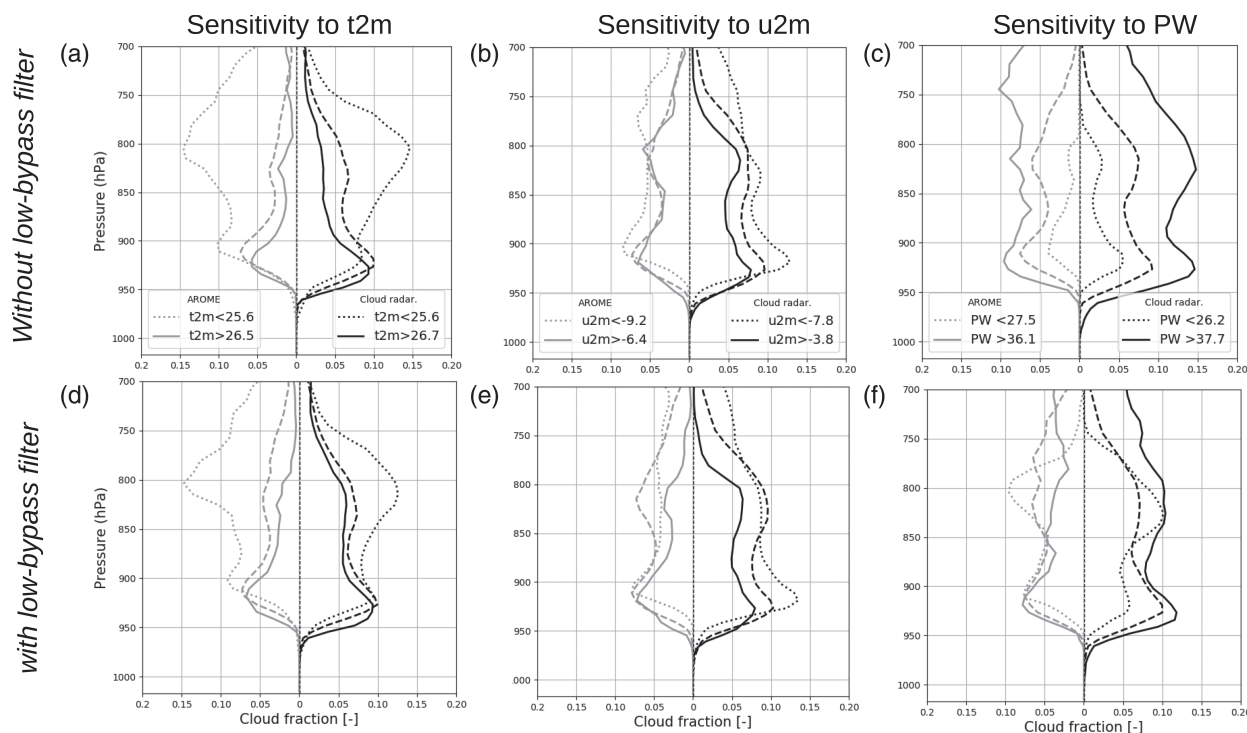


**FIGURE 6** Mean vertical profiles (January–February, 2018–2020) at the BCO of the sensitivity of the cloud fraction to the (a) surface temperature (t2m), (b) surface zonal wind speed (u2m), and (c) precipitable water (PW). For PW, estimates come from HATPRO. (d–f) same as (a–c) but for 48 hr low-pass filtered t2m, u2m, PW. The mean cloud fraction associated with the 20% lowest values (first quintile) of the distribution of each parameter is plotted on a dotted line, the 60% intermediate values on a dashed line, and the 20% highest values (last quintile) on a solid line. Note that the first quintile (20% lowest values) of u2m represents the strongest trade winds (on a dotted line)

### 3.4 | Evaluation of the environment variability on a daily to interannual scale

In the previous section, PW, u2m and t2m have been identified as large-scale parameters that greatly control the cloud fraction of the shallow convection. To gain further insight into how these parameters interplay, Figure 7 exhibits their 24 hr averaged time-evolution during three winter seasons for both observations and AROME-OM at the BCO grid point. The evaluation of the precipitation is carried out against precipitation forecasts averaged over a  $0.25^\circ$  square ahead of BCO (Figure 1b, pink square), which is equivalent to the effective resolution of the clouds. Precipitation is accumulated over a 0600–0600 UTC period.

AROME-OM captures fairly well the interannual variability of the environment at the BCO, with a relatively wet, hot and windy season in 2018 followed by a relatively dry, cool and calm season in 2019. The intraseasonal variability, with successive dry and wet events, is also well reproduced. The day-to-day variability of PW is consistent with the estimates of the microwave radiometer (Humidity And Temperature Profiler, HATPRO) and of the GNSS retrievals, except for the strongest events which are underestimated down to  $-5$  mm. Bock *et al.* (2021) highlighted the same shortcoming in the ERA5 reanalysis.

The underestimation of precipitation in AROME-OM in intermediate range of intensity (from 1 to  $10 \text{ mm}\cdot\text{day}^{-1}$ ) found by Faure *et al.* (2020) could be related to this underestimation of the peak of PW. In the absence of a strong peak of PW, as in 2019, the PW is in contrast overestimated by AROME-OM by about 1 mm. The surface wind speed is also in good agreement with the observations, except during the period of slackening of the winds (e.g. 15–17 February 2019) where the overestimation in the model reaches  $2 \text{ m}\cdot\text{s}^{-1}$ . This bias could be partly accounted for by the difference of land surface between the model and the BCO platform since the grid point in AROME-OM is located a few hundred metres away from the island. Although obviously less pronounced near the surface, the overestimation of the wind is consistent with the bias observed in radiosoundings (Figure 2) at Grantley Adams Airport. The bias in surface temperature is not significant ( $\sim -0.2 \text{ K}$ ), except during marked rainy events (e.g. 23 January 2020) with a warm bias ( $\sim +1 \text{ K}$ ) which may be related to the land surface difference between the grid point of AROME-OM and the BCO.

It is not obvious how to disentangle the interplay between PW, u2m, t2m and precipitation. The relative dry season in 2019, dominated by low PW and scarce precipitation, appears to be correlated with weak surface

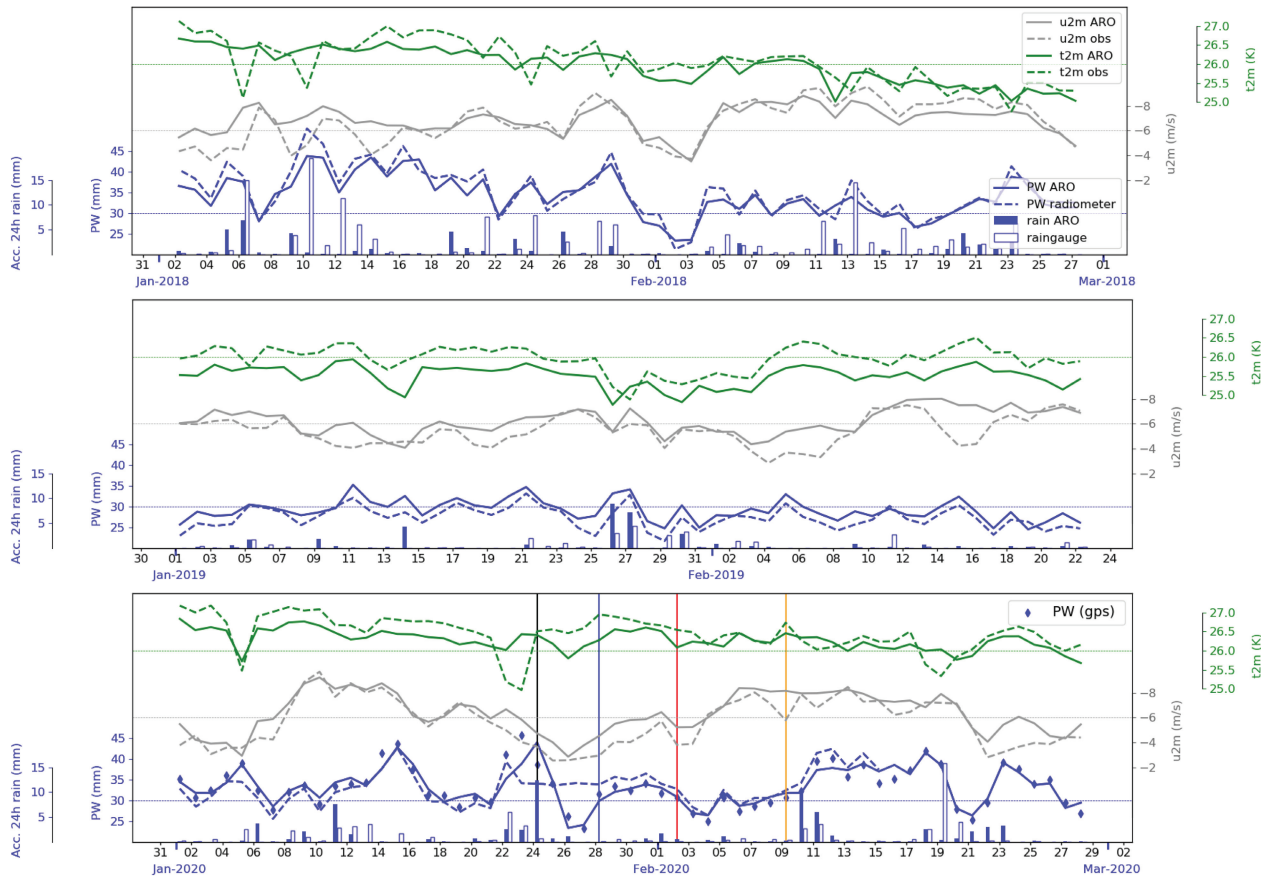


**FIGURE 7** Daily averaged time-evolution at the BCO over three winter periods (January–February, 2018–2020) for the observations (dashed line) and AROME-OM (solid line) of the precipitable water (mm, in blue), the surface zonal wind ( $\text{m}\cdot\text{s}^{-1}$ , in grey) and the surface temperature ( $^{\circ}\text{C}$ , in green). In all panels, PW estimates derived from the HATPRO radiometer are displayed with a dashed blue line. For 2020, in the lowest panel, PW estimates derived from the BCON GNSS are displayed with blue diamonds. Blue bars represent the 24 h accumulated precipitation (0600–0600 UTC) of the rain-gauge (blue solid bar) and of AROME-OM (white bar with blue edge) that have been averaged over a  $0.25^{\circ}$  square ahead of BCO (see Figure 1b). Vertical coloured (black, blue, red, orange) solid lines represent the four case-studies (fish, sugar, flower, gravel) detailed in Section 4 [Colour figure can be viewed at [wileyonlinelibrary.com](http://wileyonlinelibrary.com)]

wind speed, which corroborates the literature (Nuijens and Stevens, 2012). In 2018 and 2020, except during the periods of sudden stilling in the trade-wind regime (e.g. 1–3 February 2018), this relationship weakens. Indeed, the period of strengthening of the wind (e.g. 6–9 February 2020) is not necessarily associated with a moister environment (PW  $\sim$  32 mm). The slow decrease of PW across the season 2018 is paired with that of t2m. However, this correlation is not evident the two following years. The question of the link between precipitation occurrence and PW was raised by Neelin *et al.* (2009). They found that precipitation may be triggered above a critical value of PW which is driven by the mean layer-integrated tropospheric temperature. This threshold is around 36 mm over the Sahel in summer (Parker and Diop-Kane, 2017, their figure 3.5) whereas it drops to about 25–30 mm over the subtropical ocean in winter, which explains the high occurrence of rainy days since this threshold is often exceeded. This discussion shows how it is difficult to shed light on the

interplay of parameters that control cloud fraction. Nevertheless, the good ability of the model to reproduce their temporal variability allows us to support the results of Figure 6 concerning the sensitivity of the cloud fraction to the large-scale environment.

#### 4 | ABILITY OF AROME-OM TO REPRESENT THE DIFFERENT SHALLOW CONVECTION MESOSCALE ORGANISATIONS DURING EUREC<sup>4</sup>A

In this section, we investigate the ability of AROME-OM to reproduce the four main mesoscale cloud spatial organisations (Stevens *et al.*, 2020) and the environment in which they form, with a particular focus on four different periods selected during the EUREC<sup>4</sup>A campaign.

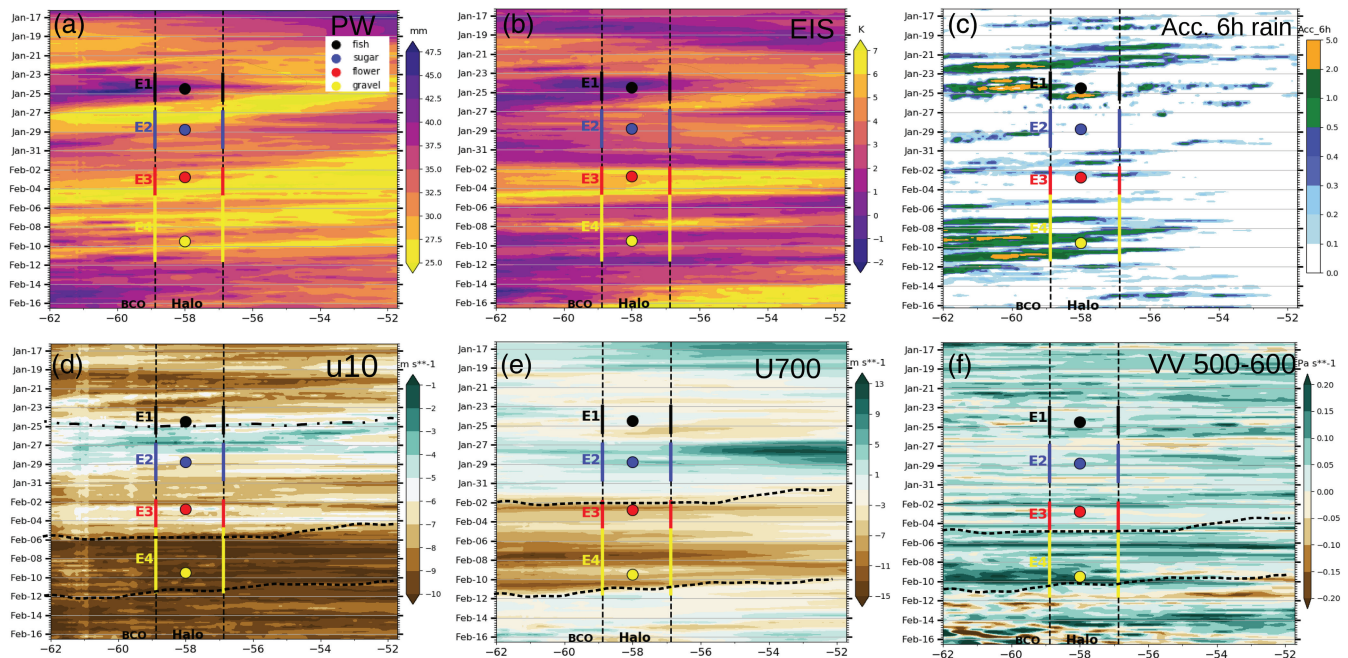


**FIGURE 8** Longitude–time diagrams over the EUREC<sup>4</sup>A’s period (16 January–16 February 2020) for the AROME-OM 6–30 hr forecasts range initiated every day at 0000 UTC of the (a) precipitable water (PW, in mm), (b) estimated inversion strength (EIS, in K), (c) 6 hr accumulated precipitation (mm), (d) surface zonal wind speed ( $u_{10}$ , in  $\text{m}\cdot\text{s}^{-1}$ ), (e) zonal wind at 700 hPa ( $U_{700}$ , in  $\text{m}\cdot\text{s}^{-1}$ ), and (f) vertical velocity averaged in the layer 500–600 hPa ( $w_{500-600}$ , in  $\text{Pa}\cdot\text{s}^{-1}$ ). Fields are averaged in the latitude band of the HALO circle extending between  $12.3^{\circ}\text{N}$ – $14.3^{\circ}\text{N}$ . (a–f) The two vertical dashed lines denote the longitudinal extension of the HALO circle. (a,b) The tongue-like structure (black solid line) outlines a period of large PW, low EIS and high precipitation. (d) The dashed-dotted line highlights the occurrence of a shear line in the zonal wind. (d,e) The dashed lines represent periods of (d,e) strong winds and (f) strong subsiding motions. Coloured dots and vertical bars mark the four case-studies and their associated environment (E1, E2, E3, E4) which are detailed in Section 4 [Colour figure can be viewed at [wileyonlinelibrary.com](http://wileyonlinelibrary.com)]

#### 4.1 | Identification of four distinct large-scale environments during EUREC<sup>4</sup>A

Figure 8 shows the AROME-OM longitudinal Hovmöller diagrams for the EUREC<sup>4</sup>A field campaign (16 January–16 February 2020) averaged on the latitude band of the HALO circle for various parameters which are likely to control the trade-wind cumuli patterns: surface wind speed, large-scale vertical velocity in the mid-troposphere ( $\omega_{500-600}$  hPa), PW and estimated inversion strength (EIS: Wood and Bretherton, 2006), defined as  $\text{EIS} = \text{LTS} - \Gamma_{850}(z_{700} - \text{LCL})$  where  $\Gamma_{850}$  is the moist-adiabatic potential temperature gradient at 850 hPa,  $z_{700}$  is the height of the 700 hPa level, and LCL is the height of the lifting condensation level. In addition, the 6 hr accumulated precipitation is shown. Focusing on the longitude of the HALO circle (in between the two vertical dashed lines), several periods showing a distinct environment can be identified:

1. From 22 to 25 January, the air mass is under the influence of an extratropical intrusion in a form of a trailing cold front, associated with both a shear line in the trade winds (Figure 8d, see the horizontal

dashed-dotted line) and an increase of PW (Figure 8a, see the tongue-like structure). Schulz *et al.* (2021) and Aemisegger *et al.* (2021) suggested that the Fish pattern frequently arises in association with this synoptic environment. The concomitant decrease of the inversion strength (Figure 8b) favours the deepening of the shallow cumulus leading to a significant precipitation event (Figure 8c). The large-scale environment of this period is called E1.

2. This disturbed period is followed for about 4 days (27–30 January) by fair weather with very shallow cumulus (see the reports from the HALO <https://observations.ipsl.fr/aeris/eurec4a/#/>). After the passage of the cold front, the depth of the trade-wind layer decreases with calm winds at the surface, and above, at 700 hPa, a regime of light westerlies occurs. A decrease in wind speed paired with a drop in surface temperature leads to a reduced latent-heat flux and a relative decrease of PW (Figure 7c, see 27 January). The joint effects of weak subsiding motion in mid-troposphere and the absence of strong inversion trades (+1 to +3 K), which prevents the spreading of the cloud tops, favours the occurrence of a field of small “popcorn” cumuli or

even a regime of suppressed clouds. This environment associated with a “pause” in the trade-wind regime is called E2.

- From 2 February, the trade-wind layer is largely modified with a sudden restoration of strong easterlies at 700 hPa (Figure 8e) associated with a deepening of the trade-wind layer and an increase of the inversion strength. However, surface easterlies remain weak for the season (Figure 8d). This “intermediate” trade-wind regime is so-called E3.
- From 5 to 11 February, the environment returns to its mean climatological features with both an increase in the surface trade winds and stronger subsiding motion in mid-troposphere coinciding with a westward extent of the subtropical North Atlantic high (not shown). This synoptic regime results in both a moistening of the boundary layer (increase of PW) and weaker inversion strength, leading to an increase in significant rainy events. This environment, more representative of a climatological “trade-wind regime”, is called E4.

## 4.2 | Selection of four cases representative of the distinct large-scale environments

We hereby investigate whether the four distinct large-scale environments (E1, E2, E3, E4) identified in the previous section can be associated with different spatial mesoscale cloud organisations observed in geostationary images (Figure 9, first line). The model shows a very good ability to reproduce the large variety of mesoscale pattern throughout the EUREC<sup>4</sup>A campaign (<https://observations.ipsl.fr/aeris/eurec4a/>) but in this study we focus on particular days for which a HALO flight has been conducted. The choice of the cases and their following description largely rely on both the HALO flight reports and the C<sup>3</sup>ONTEXT (Common Consensus on Convective OrgaNizaTion during the EUREC<sup>4</sup>A eXperiment) classification based on satellite observations (Schulz, 2022):

- The 24th January at 1200 UTC (Figure 8, black dot) is characterized by an unusually deep (4 km)

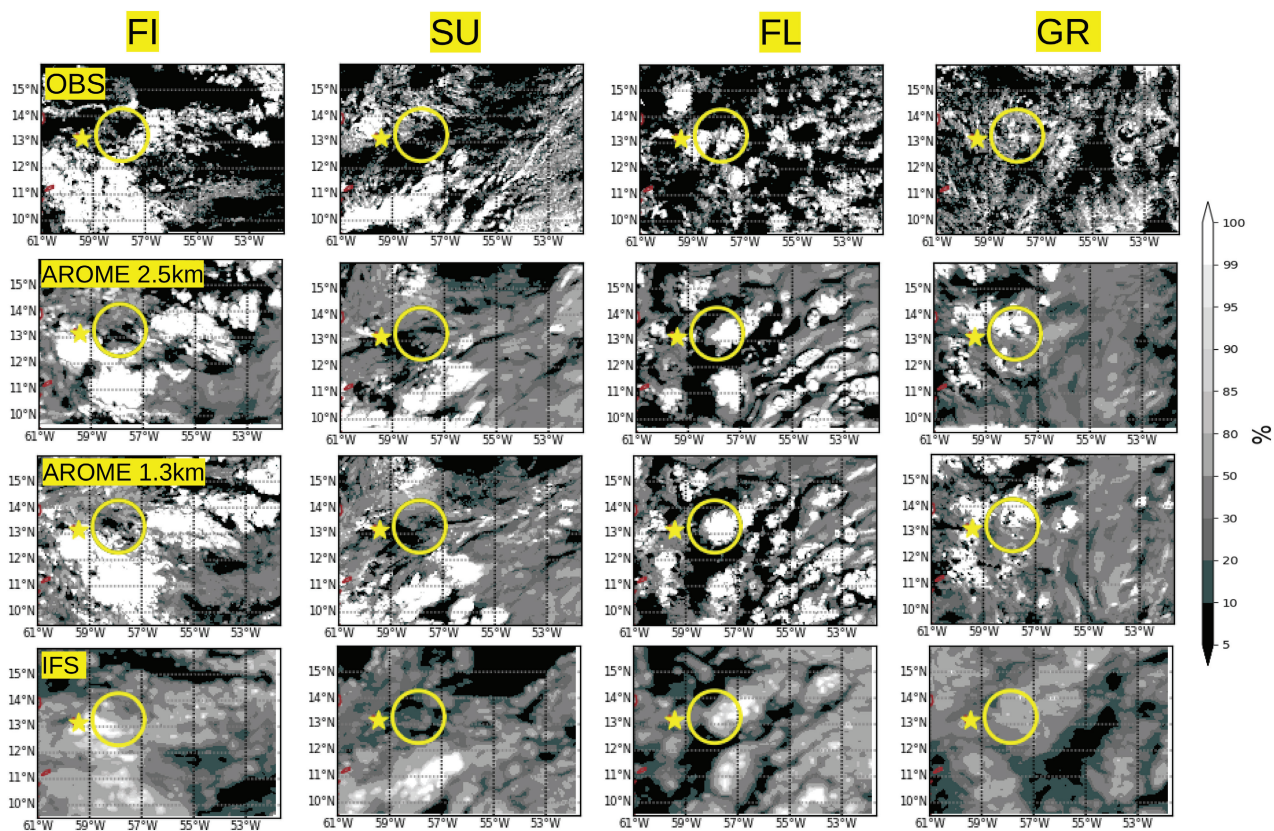


**FIGURE 9** Cloud fraction (%) for (1st column) the FI case on 24 January 2020 at 1200 UTC, (2nd column) the SU case on 28 January 1800 UTC, (3rd column) the FL case on 2 February 1800 UTC, and (4th column) the GR case on 9 February 1200 UTC. The 1st line shows the 2 km gridded field of cloud fraction (up to 450 hPa) constructed with a combination of the visible channel of GOES16 and a cloud mask from SAFNWC. The 2nd–4th lines represent the cloud fraction (up to 450 hPa) of AROME-OM at a 2.5 km resolution, AROME-OM at a 1.3 km gridded at a 2.5 km resolution, and IFS at a 12.5 km resolution, respectively. The BCO is represented by a yellow star and the HALO path by a yellow circle [Colour figure can be viewed at [wileyonlinelibrary.com](https://onlinelibrary.com)]

convection overshooting the trade-wind inversion producing extensive stratiform clouds which are the remnants of the apparent fishbone-like skeleton. The presence of an evident cold pool to the north of the HALO circle is also mentioned in the flight report. According to the classification of Stevens *et al.* (2020), the appearance of this mesoscale cloud organisation can be associated with a Fish pattern (FI in the following). Following the C<sup>3</sup>ONTEXT classification of Schulz (2022), 22nd January would appear to be a better choice for the representation of the Fish environment (E1); nevertheless, when HALO flew, the FI cloud patterns were much more prevalent on 24th February.

2. To illustrate the environment E2, the 28th January at 1800 UTC (Figure 8, blue dot) is selected. It is dominated by scattered shallow convection except in the very north with a remnant of a northwest–southeast oriented line of flower-like elements. This case is close to a Sugar cloud organisation (SU in the following).
3. For the environment E3, the 2nd February at 1800 UTC (Figure 8, red dot) is chosen. It is characterized in the vicinity of the HALO circle by the occurrence of Flowers-structure (FL in the following) associated with marked cold pools. The physical mechanisms implied in such a cloud pattern are fully documented by recent studies based on LES (Narenpitak *et al.*, 2021; Dauhut *et al.*, 2022).
4. For the environment E4, the 9th February at 1200 UTC (Figure 8, yellow dot) is selected. The scene of the HALO circle was dominated by streets of cloud cumulus in development with occasionally larger stratiform cloud aggregation associated with precipitation. This variety of vertical extension (up to 3–4 km) with clouds organized along lines, sometimes resembling cold pools, may correspond to a Gravel cloud organisation (GR in the following).

### 4.3 | Ability of AROME-OM to reproduce the four cases

The ability of AROME-OM to represent these four aforementioned cases is now assessed, both in its current configuration and in its future configuration at a 1.3 km resolution. This evaluation is also carried out against the analyses of IFS at a 12.5 km horizontal grid spacing.

Figures 9 and S1 (first row) present the cloud organisation as observed by geostationary satellite observations. Focusing on the scene of the HALO circle (Figure S1), the size of the cloud pattern depends widely on the organisations: SU is mostly populated by unorganized and very small cloud patterns, FI is dominated by large organisation

of about 100 km wide, FL is more characterized by circular clumped structures of about 50–100 km whilst GR shows more linear patterns organized along lines of a few tens of km (yellow arrows). Both configurations of AROME-OM (second and third rows) show a good ability to reproduce the main features of these distinct organisations such as the mesoscale fish-bone like structure on the southern side of the HALO circle, the apparent gust front along which FL and GR clouds pattern form (Figure S1, dashed yellow lines) as well as the large areas of clear air that surround FI and FL structures. Compared to the satellite images, the loss of accuracy in the structure of the clouds in both runs of AROME-OM is partly linked with their effective resolution which is about 22–25 km for the current configuration and 12 km for the future configuration. This is particularly evident for the finer structures such as SU and GR (Figure S1). The benefit from an increase of resolution of AROME-OM is substantial on the eastern boundary of the domain, where finer structures are better caught at a 1.3 km resolution (Figure 9). The evaluation of AROME-OM is carried out in the vicinity of the HALO circle which is quite far from the eastern side of the domain which may be strongly influenced by its forcing model. IFS partly fails to mimic the main cloud organisations (Figure 9), except for the extensive stratiform clouds or flower-like structure, highlighting the need of a kilometre-scale model to reproduce the four main mesoscale patterns described in Stevens *et al.* (2020).

In both the models and the satellite observations, the patches of cloud fraction greater than 80% (Figure 10, blue contour) roughly coincide with PW greater than 36 mm (Figure 10, in orange), especially for GR and FL cases. PW exhibits strong mesoscale variability which suggests a major role of the low-level convergence leading to a fast increase of PW, rather well captured by both versions of AROME-OM. For instance, PW in the FI case ranges from 30 mm north of the HALO circle to about 50 mm southeast. This mesoscale pattern is dominated by the most extensive patches of the highest values of PW (>50 mm) that are the footprint of the fishbone-like skeleton. The GR type is rather populated by isolated strong peaks of PW (~50 mm) that do not exceed a horizontal extension of about 10 km. FI and GR types are probably the two cases with the most extensive cloud depth. The AROME-OM vertical–longitudinal cross-section of the relative humidity (Figure S2, 2nd line) indeed reveals that the cloud-top height reaches 4 km (550/600 hPa) for FI and 5 km (500/550 hPa) for GR. Although a little overestimated, this relative deep extension of the cumulus was supported by the observations during the HALO flight. The joint examination of the spatial distribution of the cloud fraction and the PW (Figures S1 and 10)

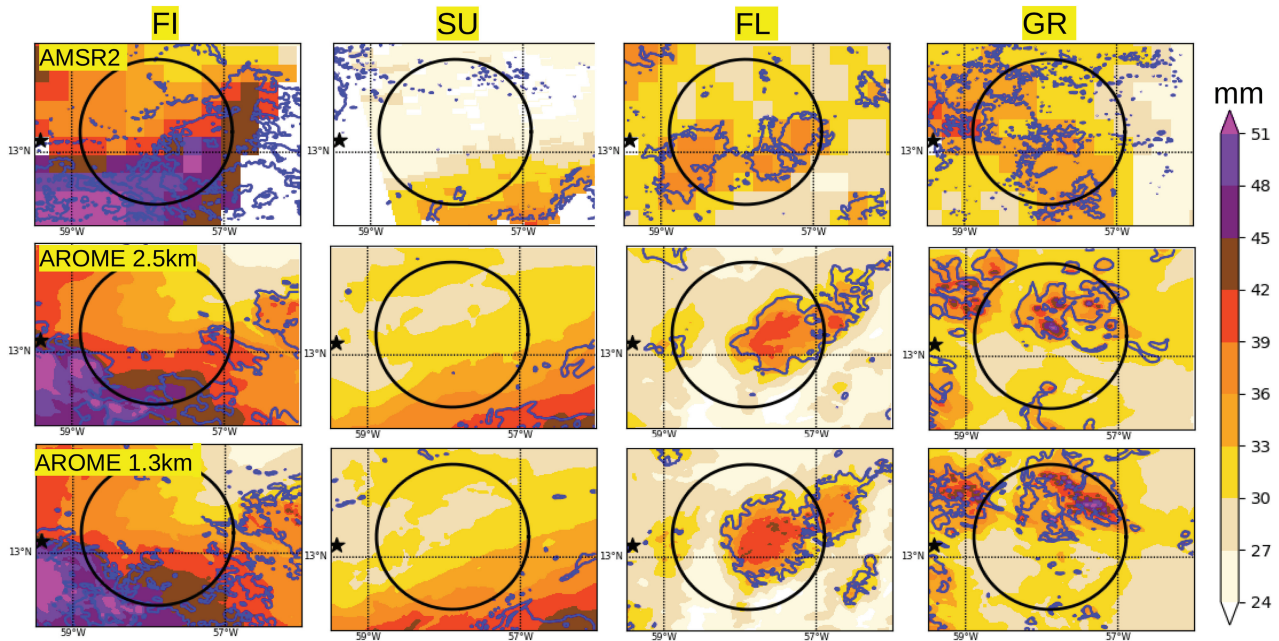


**FIGURE 10** As in Figure 9 but for the PW and focused on the HALO circle. The 1st row for the PW as measured by AMSR2 for the 24 January 2020 at 1512 UTC (FI), 28 January 1635 UTC (SU), 2 February 1657 UTC (FL) and 9 February 1703 UTC (GR). The cloud fraction greater than 80% is superimposed with a blue isoline. The BCO and the HALO path are represented by the black star and the black circle, respectively [Colour figure can be viewed at [wileyonlinelibrary.com](https://onlinelibrary.com)]

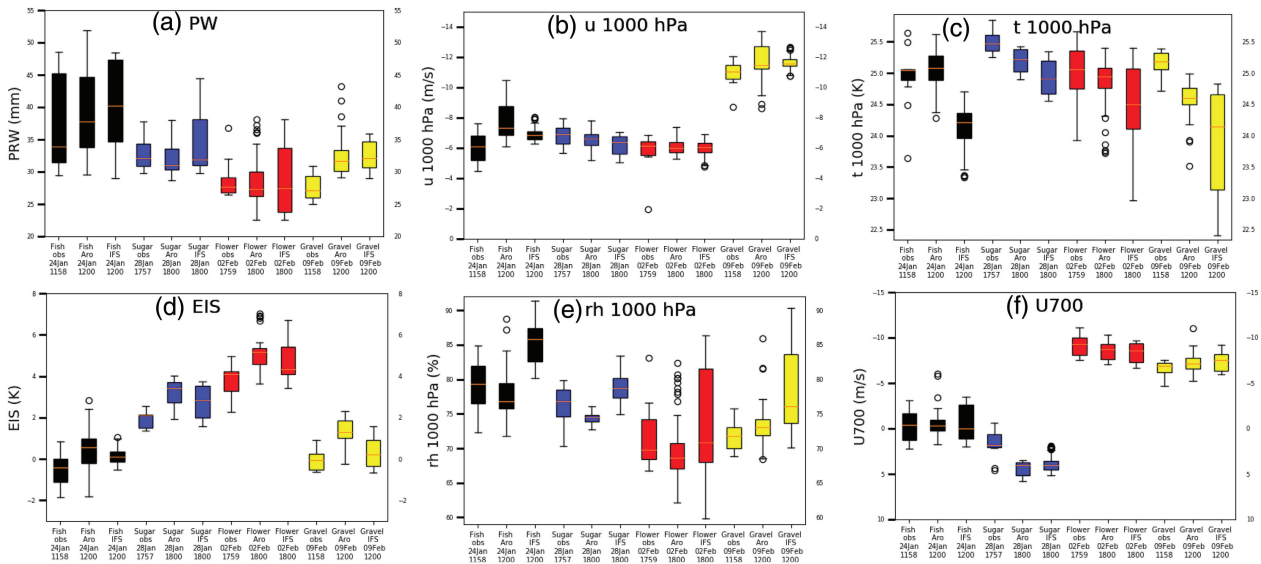
does not allow us to determine a PW threshold below which large-scale areas of suppressed clouds occur. For instance, for the SU case, the extensive area of clear sky in the region of the HALO exhibits PW ranging from 24 mm to the northeast to 36 mm to the southwest. To better understand the relationship between PW and cloud occurrence, further investigations must be undertaken. LES would be a suitable tool to disentangle the mechanisms at play and their key spatio-temporal scales. In particular, the question is open as to whether the positive anomalies in PW are due to enhanced boundary-layer convective activity, to shallow convection outflow (Bretherton and Blossey, 2017; Narenpitak *et al.*, 2021; Dauhut *et al.*, 2022), or former cloud clusters which dissipate.

#### 4.4 | Assessment of the large-scale environment during the four case-studies against the dropsondes

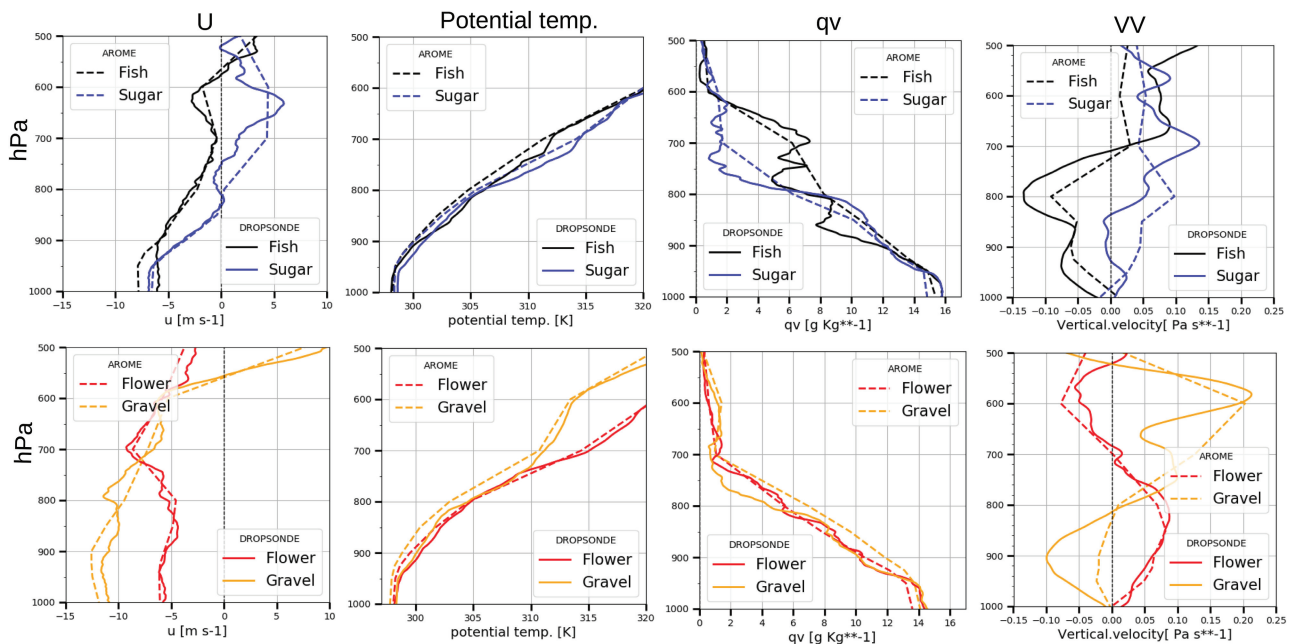
The large-scale environment in which the four cases form is assessed against a unique dataset of dropsondes launched along the HALO circle. The evaluation procedure is detailed in Section 2.3.

Figure 11 shows a comparison of the distribution of each parameter along the HALO circle for the four cases. The distribution of both AROME-OM and IFS

roughly agrees with that of dropsondes, with a little benefit for AROME-OM, for the near-surface temperature and relative humidity, as well as PW in three out of four cases. The overestimation of the inversion strength in AROME-OM ( $\sim +2$  K) appears to be partly controlled by its forcing model ( $\sim +1$  K). This may be indicative of an overestimation of the large-scale subsidence in the free troposphere but the examination of the vertical profile of the vertical velocities (Figure 12 for AROME-OM, not shown for IFS) does not allow the confirmation of this hypothesis. Similarly, the large PW overestimation in AROME-OM for FI and GR cases ( $+4$  mm) is likely driven by that of IFS ( $+5$  to  $+6$  mm), even if this bias is not observed for the two other cases. Both near-surface wind speed and near-surface temperature exhibit weak biases (resp.  $<1$  m·s<sup>-1</sup> and  $<0.5$  K) which are in good agreement with the biases found at the BCO during the three winter seasons (Figure 7). Figure 12 compares the thermodynamical profile of AROME-OM against the mean profile of about 12 dropsondes. Overall, the biases of the four cases are consistent with those previously identified in the radiosoundings at Grantley Adams Airport during the three winter seasons (2018–2020), namely a cold bias in the cloud layer ( $\sim -1$  K 930–800 hPa), a dry bias ( $\sim -1$  g·kg<sup>-1</sup>) in the sub-cloud layer as well as an overestimation of the trade winds ( $\sim 1$  m·s<sup>-1</sup>) below 850 hPa. The AROME-OM vertical velocity profiles roughly coincide with those of the dropsondes, even if the magnitude of the upward



**FIGURE 11** Distribution along the HALO path circle for the four case-studies in 2020 of the (a) PW (mm), (b) 1,000 hPa zonal wind speed ( $m \cdot s^{-1}$ ), (c) zonal wind speed at 700 hPa (U700,  $m \cdot s^{-1}$ ), (d) EIS, (e) 1,000 hPa temperature ( $^{\circ}C$ ), (f) 1,000 hPa relative humidity (%), from the JOANNE dropsonde products (obs), AROME-OM (Aro) and IFS. The FI case is displayed in black, the SU in blue, the FL in red and the GR in yellow. Orange lines represent median values and coloured box the interquartile range. Upper whiskers extend up to 1.5 times the last interquartile and lower whiskers down to 1.5 times the first interquartile [Colour figure can be viewed at [wileyonlinelibrary.com](http://wileyonlinelibrary.com)]



**FIGURE 12** Vertical profiles for the FI and SU cases (1st line) and the FL and GR cases (2nd line) of the (1st column) zonal wind (U,  $m \cdot s^{-1}$ ), (2nd column) potential temperature (K), (3rd column) specific humidity ( $q_v$ ,  $g \cdot kg^{-1}$ ), and (4th column) vertical velocity (VV,  $Pa \cdot s^{-1}$ ). Averaged over the HALO path, solid lines represent JOANNE dropsonde product and dotted lines AROME-OM [Colour figure can be viewed at [wileyonlinelibrary.com](http://wileyonlinelibrary.com)]

motion in the cloud and sub-cloud layers of the GR case is underestimated.

To summarize, in spite of weak biases, AROME-OM is able to represent the variety of large-scale environments in which the main mesoscale organisations form.

### 4.5 | Documentation of the air masses of the four case-studies

Recent investigations (Bony *et al.*, 2020; Schulz *et al.*, 2021) have shown that the near-surface wind speed and the

strength of the lower-tropospheric stability play a discriminating role in the occurrence of the mesoscale patterns in the western North Atlantic trade-wind region. This following section hereby investigates to what extent the variety of large-scale environment identified among the four case-studies adheres to these findings.

The examination of the thermodynamical profiles (Figure 12) allows us to discriminate the four cases into two thermodynamically distinct environments: a first including the FI and SU cases (so-called “FISU”) with a shallow trade-wind layer (1st line), and a second one including FL and GR cases (so-called “FLGR”) with a deep trade-wind layer penetrating up to 600 hPa (2nd line). This difference of environment occurs throughout the Caribbean domain (Figure S2, 1st line) and is rather consistent with the findings of Bony *et al.* (2020) who have shown that FL and GR tend to form when the trade winds are strong.

The FI and SU environments differ greatly in their estimated inversion strength. As discussed in Section 4.1, this FI case is driven by an extratropical wind shear line leading to an increase of low-level convergence and moistening (PW  $\sim$  40 mm, Figure 11) which in turn favours instability (EIS  $\sim$  0 K, Figure 11). The strong upward motion in the SCL (Figure 12) supports the vertical development of cumulus up to 600 hPa as exhibited on the vertical profile of specific humidity (Figure 12). In contrast to the FI case, the SU case is characterized by a somewhat stronger inversion strength (EIS  $\sim$  +2–3 K, Figure 11). Disentangling mechanisms responsible for such differences between FI and SU is rather complex, but a finer exploration of the causes of the sudden stilling in the trade-wind regime provides a hint. Here, the light winds are associated with a loose horizontal pressure gradient in relation with a westward shift of the subtropical highs over Southern Europe (not shown). In agreement with the findings of Nuijens and Stevens (2012), a slackening in the trade-wind regime is correlated with low PW (Figure 7, see between the blue vertical line and 2 days before). In turn, low PW favours both stability and subsiding motion in the SCL, as exhibited in the vertical profile. This case is consistent with the works of Bony *et al.* (2020) where during the winter 2009–2010 (their figure 4e) the SU pattern can occur in such a stable environment.

The FL and GR case environments also significantly differ by their inversion strength. The GR case arises in an unstable environment with an estimated inversion strength close to 0 (Figure 11). Examination of the vertical profile of potential temperature (Figure 12) confirms that this case is the most unstable among the four cases even if the signature of the clouds is not visible on the vertical profile of the specific humidity since no deep cumulus crosses the HALO circle but rather lies inside. The vertical

extension of cumulus up to 4 km (Figure S2,  $\sim$ 600 hPa) is probably fuelled by the occurrence of strong upward motions in the sub-cloud layer (Figure 12). The ability of the strong subsidence in mid-troposphere in patterning the mesoscale shallow convection needs more in-depth studies. In contrast to the GR case, the FL case is associated with a strong inversion strength (EIS  $\sim$  +4–5 K, Figure 11). In agreement with Schulz *et al.* (2021), the cloud top is much lower than in the GR case (Figure S2, 2nd line) and spread below a 700–750 hPa layer of strong stability (Figure 12, see potential temperature). This case exhibits significant subsiding motions in the SCL (Figure 12, red lines) which probably represent the footprint of a cold pool covering the major area of the HALO circle. In agreement with Bock *et al.* (2021), it could be hypothesized that in a windy environment the difference of organisation between FL and GR is not driven by the PW since the same amounts of PW are observed for both cases (Figure 11), which differs greatly from the environment of the FISU family where PW plays a discriminating role.

To conclude, it may be argued that AROME-OM captures the large variety of environment in which the four main organisations identified by Stevens *et al.* (2020) form. The four illustrated cases are in agreement with the past studies, except for the FI case which is characterized by a much stronger inversion strength than usually observed (Bony *et al.*, 2020, their figure 4e).

## 5 | CONCLUSIONS

The major aim of this study was to investigate the potential of the French operational convection-permitting model AROME-OM in order to represent the shallow convection in the downwind trade regime. The principal findings are based on a set of three wintertime (January–February, 2018–2020) 2.5 km resolution simulations performed across a very large domain ( $2,000 \times 1,200 \text{ km}^2$ ) with lateral boundary conditions provided by IFS. A subdomain is defined ( $1,000 \times 500 \text{ km}^2$ ) in order to take advantage of the international EUREC<sup>4</sup>A field campaign which took place to the east of Barbados in January–February 2020. In terms of observations, this study also benefits from *in situ* measurements which have been collected at the Grantley Adams Airport and at the BCO platform which are both representative of the environment in which trade-wind cumuli develop.

The evaluation of the model against the soundings of Grantley Adams Airport revealed an excessive deepening of the boundary layer leading to a cold and dry bias, along with trade winds which were too strong. One objective of this study was to investigate the ability of AROME-OM to capture the double peak of cloud fraction

(Nuijens *et al.*, 2014), with a first peak near the cloud base ( $\sim 920$  hPa) and a second peak near the top ( $\sim 820$  hPa) of the deepest cumuli. Even though the shallow convection is parametrized as in most kilometric-scale horizontal resolution models, the model shows a good ability to simulate a larger variance in cloudiness near cloud top rather than near cloud base, in agreement with observations (Schulz *et al.*, 2021). Cloud depth is overall a little underestimated in AROME-OM and the cloud fraction near the top of the deepest cumuli is too strong. This suggests that additional calibration of the vertical mixing of the shallow convection scheme which strongly affects the depth of the boundary layer (Heim *et al.*, 2021) is required. The analysis of the cloudiness sensitivity to the large-scale environment indicates a significant increase at the cloud top for colder surface temperature and low PW, which probably corresponds to FL or FI cloud organisations. In agreement with Nuijens and Stevens (2012), it has also been found that the cloud deepens in conditions of stronger winds, with the caveat that the increase of cloudiness near the cloud base is poorly represented in AROME-OM.

One may also wonder if air-mass characteristics are indicative of the different mesoscale cloud organisations. Earlier studies (Medeiros and Stevens, 2011; Bony *et al.*, 2020; Aemisegger *et al.*, 2021; Schulz *et al.*, 2021) suggested that organisation is the result of the combined effect of various parameters such as surface wind speed, lower-tropospheric stability and vertical velocity in mid-and/or low troposphere. The EUREC<sup>4</sup>A field campaign allowed us to show the good ability of AROME-OM at a 2.5 km resolution to represent the large variety of organisations that occur in boreal winter conditions in the North Atlantic trades (Stevens *et al.*, 2020). This study focuses on four case-studies that were selected during this campaign on the basis of the HALO flight reports and of the C<sup>3</sup>ONTEXT classification (Schulz, 2022). Our analysis reveals that AROME-OM gives a much better description of the cloud organisation than a model at lower resolution such as IFS for those cases. The model shows a good ability to describe the different environments in which the four cases form, in line with the EUREC<sup>4</sup>A observations, with weak biases consistent with the biases found when comparing to the long-term observations at the BCO. In agreement with past studies (Bony *et al.*, 2020; Schulz *et al.*, 2021), the FI and SU cases occur in a calm environment associated with a shallow trade-wind layer whilst the GR and FL cases arise under the influence of a windy environment characterized by a deep trade-wind layer. This study is also in phase with the work of Bock *et al.* (2021) which revealed that the amount of PW does not allow us to distinguish the patterns, except for FI. The main point of divergence with earlier studies (Bony *et al.*, 2020) is related to the FI case since it is characterised

by stability much lower than usually observed. A closely related question is how vertical velocities matters for the organisation of mesoscale shallow convection. In agreement with Dauhut *et al.* (2022), the four case-studies highlight that mesoscale vertical motions represent the imprint of the cloud systems, but the role of vertical velocities at larger scale (hundreds of km) on the cloud organisation remains an open question.

In this study, we have focused on the sensitivity of the organisation to the environment, but further work is necessary in order to explore which processes are involved in the aggregation of the shallow convection into mesoscale organisations. In particular the role of cold pools (Touzé-Peiffer *et al.*, 2021) or diabatic heating (Bretherton and Blossey, 2017) merit further investigation. The changes in organisation that occur across the subtropical Atlantic Ocean could also be explored in virtue of the use of such a kilometric convection-permitting model in order to conduct simulations over vast domains for several weeks.

## AUTHOR CONTRIBUTIONS

**Florent Beucher:** Investigation; methodology; resources; software; validation; visualization; writing – original draft; writing – review and editing. **Alex Ayet:** Investigation; writing – review and editing. **Thibaut Dauhut:** Investigation; writing – review and editing. **Dominique Bouniol:** Investigation; methodology; writing – review and editing. **Fleur Couvreur:** Investigation; methodology; writing – review and editing. **florence favot:** Resources; software. **Ghislain Faure:** Resources.

## ACKNOWLEDGEMENTS

The authors are grateful to the reviewers and Marie Lothon for their thoughtful and useful comments that have greatly improved the original manuscript, and Yohan Brunet for his contribution to this work. We also kindly thank all contributors to the datasets used in this study, which were produced as part of the EUREC<sup>4</sup>A campaign, and in particular Geet George for his JOANNE dropsonde products. Special thanks to Olivier Bock and Sabrina Schnitt for providing data from the GPS and the radiometer installed at BCO and for their useful advice. The BCO infrastructure is maintained by Ilya Serikov, Lutz Hirsch, Friedhelm Jansen, Bjoern Bruegmann, Monika Pfeiffer and Holger Linne; without them this work would not have been possible. We would like to thank Vincent Douet from AERIS and the AERIS team for their support in publishing on the website <https://observations.ipsl.fr/aeris/eurec4a/#/> the datasets, the AROME outputs at both resolutions (2.5 and 1.3 km), and the HALO flight reports associated with this article.

## ORCID

Florent Beucher  <https://orcid.org/0000-0002-1631-2450>

Fleur Couvreur  <https://orcid.org/0000-0002-8440-3362>

Dominique Bouniol  <https://orcid.org/0000-0001-9020-1719>

Thibaut Dauhut  <https://orcid.org/0000-0002-5468-3818>

Alex Ayet  <https://orcid.org/0000-0002-4044-4488>

## REFERENCES

- Aemisegger, F., Vogel, R., Graf, P., Dahinden, F., Villiger, L., Jansen, F., Bony, S., Stevens, B. and Wernli, H. (2021) How Rossby wave breaking modulates the water cycle in the North Atlantic trade wind region. *Weather and Climate Dynamics*, 2, 281–309.
- Beucher, F., Lafore, J.-P., Karbou, F. and Roca, R. (2014) High-resolution prediction of a major convective period over West Africa. *Quarterly Journal of the Royal Meteorological Society*, 140(682), 1409–1425.
- Beucher, F., Lafore, J.-P. and Chapelon, N. (2020) Simulation and analysis of the moist vortex associated with the extreme rain event of Ouagadougou in 2009. *Quarterly Journal of the Royal Meteorological Society*, 146(726), 86–104.
- Bock, O., Bossler, P., Flamant, C., Doerflinger, E., Jansen, F., Fages, R., Bony, S. and Schnitt, S. (2021) Integrated water vapour observations in the Caribbean arc from a network of ground-based GNSS receivers during EUREC<sup>4</sup>A. *Earth System Science Data*, 13, 2407–2436.
- Bony, S., Dufresne, J.-L., Le Treut, H., Morcrette, J.-J. and Senior, C. (2004) On dynamic and thermodynamic components of cloud changes. *Climate Dynamics*, 22(2), 71–86.
- Bony, S. and Stevens, B. (2019) Measuring area-averaged vertical motions with dropsondes. *Journal of the Atmospheric Sciences*, 76, 767–783.
- Bony, S., Schulz, H., Vial, J. and Stevens, B. (2020) Sugar, gravel, fish, and flowers: dependence of mesoscale patterns of trade-wind clouds on environmental conditions. *Geophysical Research Letters*, 47, e2019GL085988.
- Bouniol, D., Protat, A., Delanoë, J., Pelon, J., Piriou, J.-M., Bouysse, F., Tompkins, A.M., Wilson, D.R., Morille, Y., Haeffelin, M., O'Connor, E.J., Hogan, R.J., Illingworth, A.J., Donovan, D.P. and Baltink, H.-K. (2010) Using continuous ground-based radar and lidar measurements for evaluating the representation of clouds in four operational models. *Journal of Applied Meteorology and Climatology*, 49(9), 1971–1991.
- Bretherton, C.S. and Blossey, P.N. (2017) Understanding mesoscale aggregation of shallow cumulus convection using large-eddy simulation. *Journal of Advances in Modeling Earth Systems*, 9, 2798–2821.
- Dauhut, T., Couvreur, F., Bouniol, D., Beucher, F., Pörtge, V., Volkmer, L., Schäfer, M., Jacob, M., Wirth, M., Brilouet, P.-E. and Ayet, A. (2022) The flower trade-wind clouds are shallow mesoscale convective systems. *Quarterly Journal of the Royal Meteorological Society* in review.
- Faure, G., Chambon, P. and Brousseau, P. (2020) Operational implementation of the AROME model in the tropics: multiscale validation of rainfall forecasts. *Weather and Forecasting*, 35(2), 691–710.
- George, G., Stevens, B., Bony, S., Pincus, R., Fairall, C., Schulz, H., Kölling, T., Kalen, Q.T., Klingebiel, M., Konow, H., Lundry, A., Prange, M. and Radtke, J. (2021) JOANNE: Joint dropsonde Observations of the Atmosphere in tropical North Atlantic meso-scale Environments. *Earth System Science Data*, 13, 5253–5272. <https://doi.org/10.5194/essd-13-5253-2021>.
- Görsdorf, U., Lehmann, V., Bauer-Pfundstein, M., Peters, G., Vavriv, D., Vinogradov, V. and Volkov, V. (2015) A 35-GHz polarimetric Doppler radar for long-term observations of cloud parameters – description of system and data processing. *Journal of Atmospheric and Oceanic Technology*, 32(4), 675–690.
- Heim C., Hentgen, L., Ban, N. and Schär, C. (2021) Inter-model variability in convection-resolving simulations of subtropical marine low clouds. *Journal of the Meteorological Society of Japan, Ser. II*, 2021-062. Online ISSN 2186-9057, Print ISSN 0026-1165.
- Hogan, R.J., Jakob, C. and Illingworth, A.J. (2001) Comparison of ECMWF winter-season cloud fraction with radar-derived values. *Journal of Applied Meteorology*, 40, 513–525.
- Honnert, R. (2016) Representation of the grey zone of turbulence in the atmospheric boundary layer. *Advances in Science and Research*, 13, 63–67.
- Hourdin, F., Couvreur, F. and Menut, L. (2002) Parameterization of the dry convective boundary layer based on a mass flux representation of thermals. *Journal of the Atmospheric Sciences*, 59(6), 1105–1123.
- Imaoka, K., Kachi, M., Kasahara, M., Ito, N., Nakagawa, K. and Oki, T. (2010) Instrument performance and calibration of AMSR-E and AMSR2. *International Archives of the Photogrammetry, Remote Sensing and Spatial Information Science*, 38(8), 13–18.
- Janssens, M., Vilà-Guerau de Arellano, J., Scheffer, M., Antonissen, C., Siebesma, A.P. and Glassmeier, F. (2021) Cloud patterns in the trades have four interpretable dimensions. *Geophysical Research Letters*, 48, e2020GL091001.
- Klein, S.A. and Hartmann, D.L. (1993) The seasonal cycle of low stratiform clouds. *Journal of Climate*, 6, 1587–1606.
- Konow, H., Ewald, F., George, G., Jacob, M., Klingebiel, M., Kölling, T., Luebke, A.E., Mieslinger, T., Pörtge, V., Radtke, J. and Schäfer, M. (2021) EUREC<sup>4</sup>A's HALO. *Earth System Science Data*, 13, 5545–5563.
- Lebeaupin Brossier, C., Ducrocq, V. and Giordani, H. (2009) Two-way one-dimensional high-resolution air–sea coupled modelling applied to Mediterranean heavy rain events. *Quarterly Journal of the Royal Meteorological Society*, 135(638), 187–204.
- Lellouche, J.-M., Greiner, E., Le Galloudec, O., Garric, G., Regnier, C., Drevillon, M., Benkiran, M., Testut, C.E., Bourdalle-Badie, R., Gasparin, F. and Hernandez, O. (2018) Recent updates to the Copernicus Marine Service global ocean monitoring and forecasting real-time 1/12 high-resolution system. *Ocean Science*, 14, 1093–1126.
- Malardel, S. and Ricard, D. (2015) An alternative cell-averaged departure point reconstruction for pointwise semi-Lagrangian transport schemes. *Quarterly Journal of the Royal Meteorological Society*, 141(691), 2114–2126.
- Masson, V., Le Moigne, P., Martin, E., Faroux, S., Alias, A., Alkama, R., Belamari, S., Barbu, A., Boone, A., Bouysse, F., Brousseau, P., Brun, E., Calvet, J.-C., Carrer, D., Decharme, B., Delire, C., Donier, S., Essaouini, K., Gibelin, A.-L., Giordani, H., Habets, F., Jidane, M., Kerdraon, G., Kourzeneva, E., Lafaysse, M., Lafont, S., Lebeaupin Brossier, C., Lemonsu, A., Mahfouf, J.-F., Marguinaud, P., Mokhtari, M., Morin, S., Pigeon, G., Salgado, R., Seity, Y., Taillefer, F., Tanguy, G., Tulet, P., Vincendon, B., Vionnet, V. and Voldaire, A. (2013) The SURFEXv7.2 land and ocean surface platform for coupled or offline simulation of earth surface variables

- and fluxes. *Geoscientific Model Development*, 6, 929–960. <https://doi.org/10.5194/gmd-6-929-2013>.
- Medeiros, B. and Stevens, B. (2011) Revealing differences in GCM representations of low clouds. *Climate Dynamics*, 36, 385–399.
- Medeiros, B. and Nuijens, L. (2016) Clouds at Barbados are representative of clouds across the trade wind regions in observations and climate models. *Proceedings of the National Academy of Sciences*, 113(22), E3062–E3070. <https://doi.org/10.1073/pnas.1521494113>.
- Narenpitak, P., Kazil, J., Yamaguchi, T., Quinn, P. and Feingold, G. (2021) From sugar to flowers: a transition of shallow cumulus organization during ATOMIC. *Journal of Advances in Modeling Earth Systems*, 13, e2021MS002619.
- Neelin, J.D., Peters, O. and Hales, K. (2009) The transition to strong convection. *Journal of the Atmospheric Sciences*, 66, 2367–2384.
- Nuijens, L. and Stevens, B. (2012) The influence of wind speed on shallow marine cumulus convection. *Journal of the Atmospheric Sciences*, 69, 168–184.
- Nuijens, L., Serikov, I., Hirsch, L., Lonitz, K. and Stevens, B. (2014) The distribution and variability of low-level cloud in the North Atlantic trades. *Quarterly Journal of the Royal Meteorological Society*, 140(684), 2364–2374.
- Nuijens, L., Medeiros, B., Sandu, I. and Ahlgrimm, M. (2015) The behavior of trade-wind cloudiness in observations and models: the major cloud components and their variability. *Journal of Advances in Modeling Earth Systems*, 7, 600–616.
- Parker, D.J. and Diop-Kane, M. (Eds.). (2017) *Meteorology of Tropical West Africa: The forecaster's handbook*. West Sussex: Wiley-Blackwell.
- Pergaud, J., Masson, V., Malardel, S. and Couvreux, F. (2009) A parameterization of dry thermals and shallow cumuli for mesoscale numerical weather prediction. *Boundary-Layer Meteorology*, 132, 83–106.
- Rasp, S., Schulz, H., Bony, S. and Stevens, B. (2020) Combining crowdsourcing and deep learning to explore the mesoscale organization of shallow convection. *Bulletin of the American Meteorological Society*, 101(11), E1980–E1995.
- Ricard, D., Lac, C., Riette, S., Legrand, R. and Mary, A. (2013) Kinetic energy spectra characteristics of two convection-permitting limited-area models AROME and Meso-NH. *Quarterly Journal of the Royal Meteorological Society*, 139(674), 1327–1341.
- Rio, C. and Hourdin, F. (2008) A thermal plume model for the convective boundary layer: representation of cumulus clouds. *Journal of the Atmospheric Sciences*, 65(2), 407–425.
- Savazzi, A.C.M., Nuijens, L., Sandu, I., George, G. and Bechtold, P. (2022) The representation of winds in the lower troposphere in ECMWF forecasts and reanalyses during the EUREC<sup>4</sup>A field campaign. *Atmospheric Chemistry and Physics Discussions*, 1–29. In review. <https://doi.org/10.5194/acp-2021-1050>.
- Schnitt, S., Löhnert, U. and Preusker, R. (2020) Potential of dual-frequency radar and microwave radiometer synergy for water vapor profiling in the cloudy trade wind environment. *Journal of Atmospheric and Oceanic Technology*, 37, 1973–1986.
- Schulz, H., Eastman, R. and Stevens, B. (2021) Characterization and evolution of organized shallow convection in the downstream North Atlantic trades. *Journal of Geophysical Research: Atmospheres*, 126(17), e2021JD034575.
- Schulz, H. (2022) C<sup>3</sup>ONTEXT: a Common Consensus on Convective OrganizaTion during the EUREC<sup>4</sup>A eXperiment. *Earth System Science Data*, 14, 1233–1256.
- Seity, Y., Brousseau, P., Malardel, S., Hello, G., Bénard, P., Bouttier, F., Lac, C. and Masson, V. (2011) The AROME-France convective-scale operational model. *Monthly Weather Review*, 139(3), 976–991.
- Sherwood, S.C., Bony, S. and Dufresne, J.-L. (2014) Spread in model climate sensitivity traced to atmospheric convective mixing. *Nature*, 505(7481), 37–42.
- Stevens, B., Ackerman, A.S., Albrecht, B.A., Brown, A.R., Chlond, A., Cuxart, J., Duynkerke, P.G., Lewellen, D.C., Macvean, M.K., Neggers, R.A.J., Sánchez, E., Siebesma, A.P. and Stevens, D.E. (2001) Simulations of trade-wind cumuli under a strong inversion. *Journal of the Atmospheric Sciences*, 58, 1870–1891.
- Stevens, B., Farrell, D., Hirsch, L., Jansen, F., Nuijens, L., Serikov, I., Brüggemann, B., Forde, M., Linne, H., Lonitz, K. and Prospero, J.M. (2016) The Barbados Cloud Observatory: anchoring investigations of clouds and circulation on the edge of the ITCZ. *Bulletin of the American Meteorological Society*, 97(5), 787–801.
- Stevens, B., Bony, S., Brogniez, H., Hentgen, L., Hohenegger, C., Kiemle, C., L'Ecuyer, T.S., Naumann, A.K., Schulz, H., Siebesma, P.A., Vial, J., Winker, D.M. and Zuidema, P. (2020) Sugar, gravel, fish and flowers: mesoscale cloud patterns in the trade winds. *Quarterly Journal of the Royal Meteorological Society*, 146(726), 141–152.
- Stevens, B., Bony, S., Farrell, D., Ament, F., Blyth, A. and Fairall, C. (2021) EUREC<sup>4</sup>A. *Earth System Science Data Discussions*, 2021, 1–78.
- Tiedtke, M. (1989) A comprehensive mass flux scheme for cumulus parameterization in large-scale models. *Monthly Weather Review*, 117(8), 1779–1800.
- Touzé-Peiffer, L., Vogel, R. and Rochetin, N. (2021) Detecting cold pools from soundings during EUREC<sup>4</sup>A. In review. <https://doi.org/10.48550/arXiv.2104.09146>.
- Vogel, R., Nuijens, L. and Stevens, B. (2020) Influence of deepening and mesoscale organization of shallow convection on stratiform cloudiness in the downstream trades. *Quarterly Journal of the Royal Meteorological Society*, 146(726), 174–185.
- Wentz, F. J. and T. Meissner. (2000) *AMSR Ocean algorithm, version 2*. Remote Sensing Systems Technical Report 121599A-1, 66 pp. Available online at <http://eospsoc.gsfc.nasa.gov/sites/default/>.
- Wood, R. and Bretherton, C.S. (2006) On the relationship between stratiform low cloud cover and lower-tropospheric stability. *Journal of Climate*, 19(24), 6425–6432.

## SUPPORTING INFORMATION

Additional supporting information can be found online in the Supporting Information section at the end of this article.

**How to cite this article:** Beucher, F., Couvreux, F., Bouniol, D., Faure, G., Favot, F., Dauhut, T. *et al.* (2022) Process-oriented evaluation of the oversea AROME configuration: Focus on the representation of cloud organisation. *Quarterly Journal of the Royal Meteorological Society*, 1–19. Available from: <https://doi.org/10.1002/qj.4354>